Title
Digital Rock Studies of Tight Porous Media

Author
Silin, D.

Publication Date
2012-08-01

Digital rock studies of tight porous media

Dmitriy Silin

Earth Sciences Division
Ernest Orlando Lawrence Berkeley National Laboratory
1 Cyclotron Road, MS 90R1116
Berkeley, CA
94720, USA

August 7, 2012

Abstract. This technical report summarizes some recently developed approaches to studies of rock properties at a pore scale. Digital rock approach is complementary to laboratory and field studies. It can be especially helpful in situations where experimental data are uncertain, or are difficult or impossible to obtain. Digitized binary images of the pore geometries of natural rocks obtained by different imaging techniques are the input data. Computer-generated models of natural rocks can be used instead of images in a case where microtomography data are unavailable, or the resolution of the tools is insufficient to adequately characterize the features of interest. Simulations of creeping viscous flow in pores produce estimates of Darcy permeability. Maximal Inscribed Spheres calculations estimate two-phase fluid distribution in capillary equilibrium. A combination of both produce relative permeability curves. Computer-generated rock models were employed to study two-phase properties of fractured rocks, or tight sands with slit-like pores, too narrow to be characterized with micro-tomography. Various scenarios can simulate different fluid displacement mechanisms, from piston-like drainage to liquid dropout at the dew point.

A finite differences discretization of Stokes equation is developed to simulate flow in the pore space of natural rocks. The numerical schemes are capable to handle both no-slip and slippage flows. An upscaling procedure estimates the permeability by subsampling a large data set. Capillary equilibrium and capillary pressure curves are efficiently estimated with the method of maximal inscribed spheres both an arbitrary contact angle. The algorithms can handle gigobytes of data on a desktop workstation. Customized QuickHull algorithms model natural rocks. Capillary pressure curves evaluated from computer-generated images mimic those obtained for microtomography data.

Contents

1. INTRODUCTION

The core of *digital rock* approach consists of computer-assisted studies of rock properties from pore-scale description obtained by various imaging techniques including micro-computed tomography (micro-CT) [4, 16, 67], focused ion-beam and scanning electron microscopy (FIB/SEM) [69, 70]. Computer-generated data mimicking natural structures also can be used as the source of input data [35, 46]. The digital rock approach is a new and in active development [47, 50, 54]. The range of properties and processes addressed by digital rock methods is very broad. Flow and elastic properties of natural rocks, geochemical processes of mineralization and contaminant transport, electric conductivity, all can be studied either individually or coupled.

The classical work [45] by Muskat and Meres mentioned that "Insofar as the flow [...] is microscopically viscous and streamline in character, it is, in principle, subject to complete description by the laws of the classical hydrodynamics, as contained in the Stokes–Navier equations. However, the obvious futility of attempting to solve these equations for the multiply connected passages composed of the pores of a porous medium has necessitated a direct empirical solution of the problem". The progress in computed tomography during past decades made possible to obtain detailed high-resolution images describing the complexity of the pore space in natural rocks. The growth of computer power makes possible to evaluate flow properties of the rock samples numerically. In case where core measurements are unreliable time-consuming and expensive, flow simulations can be run in relatively short time on numerous data sets. Although digital rock methods do not replace experiment and laboratory measurements, they can help to reduce uncertainties and play various "what if" scenarios in wide range of physical conditions [54].

Over a long period of time, flow simulations on pore networks was the standard approach to flow modeling at a microscopic scale [5, 8, 22, 24, 48]. A pore network is a graph of pore bodies connected by pore throats. The simplified geometry of such a representation of the pore space makes possible development of efficient computational algorithms. However, extraction of a network adequately describing the complexity of the pore space of natural rock is problematic. The available algorithms are computationally intensive and involve numerous tunable parameters. Thus, even though flow simulations on the 3D microtomography data is significantly more demanding computationally, it is attractive since it analyses the complexity of the pore-space geometry directly.

In this study, we employ finite-differences discretization of the Stokes equations of creeping viscous flow on the digitized pore space domain. We implement customized modifications of the two methods by A.Chorin [12, 13] to simulate flow in three orthogonal directions, and estimate the tensor of permeability by averaging the flows. Sparse matrix library [19] was employed for solving linear systems of equations.

Alternatively to finite-differences (FD) flow simulations, Lattice-Boltzmann (LBM) and finite elements (FE) methods are also reported in the literature [26, 36, 43]. A comparison between the FD, FE, and LBM approaches does not single out a clear winner [27, 42]. The choice of FD in this study was motivated by its capability to rigorously account for the boundary conditions, including flow with slippage.

In addition to pore-scale simulations, we develop an upscaling routine allowing for evaluation of an effective permeability tensor for a medium consisting of a three-dimensional rectangular grid of blocks of different permeabilities. The permeability of each block is characterized by a tensor. The permeability of the entire domain is determined by solving steady-state Darcy flow equation with Dirichlet pressure boundary condition. In addition to the heterogeneity, the solution method should also handle full permeability tensor. To solve such an upscaling problem, we employ a customized version of support-operators method [25, 58, 60].

This upscaling method makes possible evaluation of the permeability of a large domain by solving a series of smaller problems. Solving Stokes equations on smaller domains facilitates the convergence of the iterative procedures. The total computational complexity of the problem can be reduced. The simulations on different elements of the partition are independent of each other, so this part of the algorithm can be naturally parallelized. In fact, flow simulations for different domains are entirely independent of each other and can be performed on different workstations not necessarily connected into a cluster.

To evaluate relative permeability curves, the absolute permeability estimates can be combined with maximal inscribed sphere computations [59, 65]. First, the fluid distribution is evaluated for a number of capillary pressures. Then, the flow simulations are performed separately for each fluid on the part of the pore space occupied by it. Such an approach produces a reasonable estimate of relative permeability curves in capillary equilibrium [62].

The paper is organized as follows. In Section 2, we briefly review the derivation of the steady-state flow equations of incompressible fluid with no-slip and slippage boundary conditions at the pore walls. In Section 3, we discuss the discretization of Stokes equations. Section 4 describes discretization of the boundary conditions, both at the pore walls and at the boundary of the image. Finally, in Section 6, the upscaling procedure is constructed based on the support-operators method.

2. Steady flow of incompressible viscous fluid

2.1. **Flow equations.** This Section overviews the Stokes equations characterizing creeping flow of incompressible viscous fluid. The derivation of Stokes equations is described, for example, in [39]. Consider a small volume of fluid V with boundary ∂V. If $v = v(t, \mathbf{r})$ is the fluid flow velocity at time t at given location $\mathbf{r} = (x, y, z)$, then the total fluid flux through the boundary ∂V can be expressed through a surface integral

$$f(V) = \int_{\partial V} \varrho v \cdot n \, ds \tag{1}$$

where ϱ is the fluid density and $n\,ds$ is surface element with an external unit normal vector n. In absence of sinks and sources and taking into account the fluid incompressibility, by shrinking V into a point, one obtains

$$\nabla \cdot v = 0 \tag{2}$$

Equation (2) must be complemented by a momentum balance equation. The rate of variation of the total momentum of the fluid inside the volume V is determined by (a) the fluid flow across the boundary ∂V, which brings slower or faster particles in and out the volume V, (b) the stresses acting on the surface ∂V, and (c) the body forces $\mathcal{F}$, like gravity or electrostatic field, acting on the portion of fluid instantaneously locked in volume V. Thus, one obtains

$$\frac{d}{dt} (\varrho v) = - \int_{\partial V} \varrho v (v \cdot n) \, ds + \int_{\partial V} T n \, ds + \int_{V} \mathcal{F} \, dV \tag{3}$$

where T is the stress tensor. The latter is the sum of two components: pressure, pI, where I is an identity tensor, and viscous friction S resulting from the interaction between layers of fluid mowing with different velocities

$$T = -pI + T_S \tag{4}$$

The viscous stress tensor depends on the velocity gradient ∇v. This dependence is linear for a Newtonian fluid.

Both T_S and ∇v are 3×3 tensors. A general linear relationship between two such tensors involves 81 coefficients. However, not always different velocities in different layers cause friction. An example of such flow is fluid circulation around an axis at a constant angular velocity. Also, taking into account the isotropy and homogeneity of the fluid, one reduces the number of coefficients to two. The viscosity stress is presented in the form

$$S = \eta \left\{ T_{Si,j} \right\} + \zeta \nabla \cdot v I \tag{5}$$

where

$$T_{Si,j} = \begin{cases} \dfrac{\partial v_i}{\partial x_j} + \dfrac{\partial v_j}{\partial x_i}, & i \neq j \\[2ex] 2\dfrac{\partial v_i}{\partial x_i} - \dfrac{2}{3}\nabla \cdot v, & i = j \end{cases} \tag{6}$$

is the shear viscosity component. The η and ζ are, respectively, the coefficients of shear and bulk viscosity. Equations (5)–(6) can be slightly rearranged. The shear stress is a linear function of velocity gradient (or Jacobian) ∇v. This gradient itself is a second-order tensor, which can be represented as the sum of symmetric and anti-symmetric tensors. The anti-symmetric term is dropped because the rotations are irrelevant for viscose friction. The symmetric component of the tensor consists of the elements

$$\frac{1}{2}\left(\frac{\partial v_i}{\partial x_j} + \frac{\partial v_j}{\partial x_i}\right)$$

In incompressible flow, the bulk viscosity term in Eq. (5) vanishes. The same holds true for the divergence term in Equation (6) (see Eq. (2)). Thus, a substitution of equations (5)–(6) into Eq. (3) and passing to the limit as the domain V shrinks into a point yields Navier-Stokes equations of flow of viscous incompressible fluid

$$\frac{\partial}{\partial t}v + (v \cdot \nabla)v = -\frac{1}{\varrho}\nabla p + \nu\nabla^2 v + \mathcal{F} \tag{7}$$

where $\nu = \eta/\varrho$ is the coefficient of kinematic viscosity. In steady-state flow, the time derivative vanishes:

$$(v \cdot \nabla)v = -\frac{1}{\varrho}\nabla p + \nu\nabla^2 v + \mathcal{F} \tag{8}$$

The last equation is further simplified by neglecting he nonlinear with respect to v term on the left-hand side for small velocities (creeping flow assumption).The body force, $\mathcal{F}$, is assumed to have only a potential component and can be integrated into the pressure gradient term. Thus, we arrive at Stokes equations in the form

$$\eta\nabla^2 v = \nabla p \tag{9}$$

2.2. **Gas flow with slippage.** No-slip viscous-flow description of gas transport in tight porous media can be insufficient. If the gas is rarefied or the flow channels are small and narrow then slippage mechanisms or diffusion may become important. Roy *et al* [52, Figure 1] specify several flow regimes: no-slip viscous flow governed by Navier–Stokes equations, viscous flow with slippage, and diffusion flow governed by Burnett equations [11]. The criterion for applicability of specific flow model is the magnitude of the ratio of the mean free path and linear dimensions of the domain, which is the Knudsen number discussed below. Some researcher conclude that gas flow in shales can be affected by slippage and diffusion mechanisms [14, 33]. This section focuses on viscous gas flow with slippage. Slippage is sometimes used for pore-scale interpretation of the Klinkenberg effect [37] of pressure-dependent permeability to gas.

One of the differences between liquid and gas states of matter is that in gas molecules are packed less densely. The molecules move around with a speed determined by the temperature and collide with each other. The average distance travelled by a molecule between collisions is called mean free path. In ideal gas, the mean free path is infinite. Ideal gas can be a reasonable model for relatively low pressures. However, as the density of the gas grows with increasing pressure, the molecules collide more frequently and the ideal gas model becomes inadequate. The average number of collisions experienced by a molecule per unit time, Γ, is given by

$$\Gamma = \xi' n\pi\sigma^2\Omega \tag{10}$$

where n is the number of molecules in a unit volume, σ is the molecular diameter, and Ω is the mean velocity. This formula is based on a spherical model of a molecule [30]. The effective radius, σ, is of the order of 10 Å, where 1 Å $= 10^{-10}$ m. The predicted value of the dimensionless parameter ξ' is different depending on the statistical model of the distribution of velocities. For the Maxwellian distribution, $\xi' = \sqrt{2}$. The mean velocity for this distribution equals

$$\Omega = \sqrt{\frac{8\pi}{mkT}} \tag{11}$$

where T is the absolute temperature, m is the molecular mass, and k is the Boltzmann constant: $k = 1.3806503 \times 10^{-23}$ JK^{-1}.

At a given temperature, the frequency of collisions between the molecules can be characterized by mean free path, l. Clearly, $\Gamma = \Omega/l$. Thus,

$$l = \frac{1}{\xi' n \pi \sigma^2} \tag{12}$$

From the ideal gas equation of state, $p = nkT$, where p is the gas pressure. Thus, for the ideal gas model,

$$l = \frac{kT}{\xi' p \pi \sigma^2} \tag{13}$$

In other words, at a fixed temperature, the mean free path is inversely proportional to the pressure.

For example, assume a 1 km ($\approx$ 3300 ft) deep reservoir with pore pressure of 100 atm ($\approx$ 1500 psi) at a temperature near 400 K ($\approx$ 260 F). A substitution of the numbers yields a mean free path estimate at $l \approx 1.24$ Å.

The coefficient D of molecular self-diffusion, that is redistribution of the gas molecules due to the gradient of concentration of the molecules, ∇n, also can be expressed through the mean free path and mean velocity:

$$D = \frac{1}{3} l \Omega = \frac{\Omega}{3\xi' n \pi \sigma^2} \tag{14}$$

In particular, the coefficient of diffusion is a function of concentration. The redistribution of the gas molecules concentration by diffusion is not a part of the dynamic flow covered by Navier–Stokes equations. So the total gas flow is a superposition of both. Normally, the diffusion component of flow is negligible relative to the dynamic flow. However, it may be not so if the domain where the flow occurs is small enough, so that its linear dimensions are comparable with the mean free path. In such a case, diffusion may become the main mechanism of flow and must be rigorously taken into account. Such a situation can be characterized by a dimensionless ratio of the mean free path and a characteristic length scale, L, called Knudsen number

$$\mathrm{Kn} = \frac{l}{L} = \frac{1}{\xi' n \pi \sigma^2 L} \tag{15}$$

An example of such situation is flow of gas in a tight reservoir with extremely small pores [23][1]. The threshold between diffusive and classical flow regimes suggested in the literature [7] is between $\mathrm{Kn} \sim 10^{-3}$ and $\mathrm{Kn} \sim 10^{-2}$.

The molecular density n in Equation (15) is a function of pressure. The gas in reservoir conditions is stored compressed, and the magnitude of Knudsen number may be not as large as in rarefied gas flow. Some recent studies mention alternative to Maxwell's slippage mechanisms. For example, the wettability can play a role [71, 72]. Natural rocks usually are not gas-wet, that is, it is more likely that the solid grains will establish a direct contact with any reservoir fluid, but gas. Although it is not the case for kerogen inclusions capable to adsorb methane molecules [9, 10, 20, 21, 51, 66], in

---

[1] Another situation where Knudsen number is comparable with unity is flow of rarefied gas. Rarefied gas dynamics has been extensively studied in the literature [38].

tight sands the gas most likely flows in pores with not gas-wet walls or pores covered by a wetting-liquid film, which would serve as a lubricant. To summarize, the physics of slippage in gas flow may need further theoretical and experimental study.

2.3. Boundary condition.

In liquid flow, the liquid molecules stick to the bounding walls implying no-slip boundary conditions [39]. Ideal elastic collisions between gas molecules and an ideal smooth surface result in no energy loss. The molecules merely bounce from the walls imposing no shear stress on the bulk gas flow. However a real surface is not smooth, which needs to be taken into account for adequate modeling. Maxwell [44] has derived partial slip boundary conditions for gas from the kinetic theory. In partial slip, the tangential component of gas velocity, v_τ, near the wall satisfies the following relationship:

$$v_\tau = G \frac{\partial v_\tau}{\partial n} \tag{16}$$

where G is the slip factor and $\partial/\partial n$ denotes the normal derivative. Some generalizations of condition (16) resulted in higher-order slip conditions [18] and slip conditions in a tensorial form for a case where the surface roughness is anisotropic [73].

Although Maxwell's condition was originally derived for flow of rarefied gas, it is applied to flow in a micro-channel as well [7]. According to Maxwell's theory of gas slip, some gas molecules hit and bounce off the wall in an elastic manners. These molecules preserve the mean tangential component of velocity v_τ. However a fraction of molecules, denoted by f, $0 < f < 1$, experiences multiple collisions with the wall due to its roughness. These molecules eventually bounce off from the wall, but they loose the tangential component of the velocity due to multiple collisions. The wall adsorbs the tangential component of the velocity. In experiments, the magnitude of f was found between 0.2 and 1, where the lower boundary $f = 0.2$ corresponds to a very smooth wall. Calculations yield the following formula for the slip factor:

$$G = \frac{2}{3}\left(\frac{2}{f} - 1\right) l \tag{17}$$

see [44].

2.3.1. *Example: flow between parallel planes.*

Consider a pressure-driven steady flow of gas between two infinite planes. Let L denote the distance between the planes, the planes are orthogonal to coordinate z and the flow is in direction x. We assume that Navier–Stokes equations adequately describe the bulk flow, and slippage equation (16) describes the boundary conditions. Thus, one arrives at the following boundary-value problem

$$\begin{aligned} \frac{\partial^2 v_x}{\partial z^2} &= \frac{1}{\mu}\frac{\partial p}{\partial x} \\ v_x\big|_{z=0} &= G\frac{\partial v_x}{\partial z}\bigg|_{z=0} \\ v_x\big|_{z=L} &= -G\frac{\partial v_x}{\partial z}\bigg|_{z=L} \end{aligned} \tag{18}$$

Here μ is the viscosity of the gas. In dimensionless form,

$$\begin{aligned}\frac{\partial^2 V_x}{\partial \xi^2} &= \mathrm{Re}\frac{\partial P}{\partial \zeta} \\ V_x|_{\xi=0} &= G_*\frac{\partial V_x}{\partial \xi}\bigg|_{\xi=0} \\ V_x|_{\xi=1} &= -G_*\frac{\partial V_x}{\partial \xi}\bigg|_{\xi=1}\end{aligned} \tag{19}$$

Here $z = L\xi$, $x = L\zeta$, $G = G_* L$, $v_x = V_0 V$, where V_0 is a characteristic flow velocity, $p = \varrho V_0^2 P$, where ϱ is the density of the gas, and $\mathrm{Re} = \dfrac{\varrho L V_0}{\mu}$ is the Reynolds number. The solution is given by the formula

$$V = \frac{1}{2}\mathrm{Re}\frac{\partial P}{\partial \zeta}\left(\xi^2 - \xi\right) - \frac{1}{2}G_*\mathrm{Re}\frac{\partial P}{\partial \zeta} = \frac{1}{2}\mathrm{Re}\frac{\partial P}{\partial \zeta}\left(\xi^2 - \xi - G_*\right) \tag{20}$$

Thus, the dimensionless velocity at the boundary is

$$V|_{\xi=0,\,\xi=1} = -\frac{1}{2}G_*\mathrm{Re}\frac{\partial P}{\partial \zeta} \tag{21}$$

In physical variables,

$$v_x = \frac{1}{2}\frac{1}{\mu}\frac{\partial p}{\partial x}\left(z^2 - Lz\right) - \frac{1}{2}\frac{LG}{\mu}\frac{\partial p}{\partial x} = \frac{1}{2}\frac{1}{\mu}\frac{\partial p}{\partial x}\left(z^2 - Lz - LG\right) \tag{22}$$

and at the boundary,

$$v_x|_{z=0,\,z=L} = -\frac{1}{2}\frac{LG}{\mu}\frac{\partial p}{\partial x} \tag{23}$$

For the flux, one obtains

$$f_x = \frac{1}{L}\int_0^L v_x\,dx = -\frac{L^2}{12\mu}\left(1 + \frac{6G}{L}\right)\frac{\partial p}{\partial x} = -\frac{L^2}{12\mu}\left(1 + G_*\mathrm{Kn}\right)\frac{\partial p}{\partial x} \tag{24}$$

The additional term G_* on the right-hand side of the last equation describes the permeability enhancement by slippage in a slit-like pore.

2.3.2. *Example: flow in a cylindrical capillary tube.* Under similar assumptions, steady gas flow in a cylindrical tube is described in cylindrical coordinates r, θ, where r is the distance from the axis of the tube, and θ is the angle, by the following boundary-value problem:

$$\begin{aligned}\frac{1}{r}\frac{\partial}{\partial r}\left(r\frac{\partial v_x}{\partial r}\right) &= \frac{1}{\mu}\frac{\partial p}{\partial x} \\ v_x|_{r=R} &= G\frac{\partial v_x}{\partial r}\bigg|_{r=R}\end{aligned} \tag{25}$$

We assume that the axis x is aligned with the tube. The radius of the pipe must be large enough to justify application of the Maxwell's slip condition [44] for a non-flat boundary. The solution is given by

$$v_x = -\frac{1}{4}\frac{1}{\mu}\frac{\partial p}{\partial x}\left(R^2 - r^2 + 2GR\right) \tag{26}$$

Thus, the velocity at the boundary is

$$v_x = -\frac{GR}{2}\frac{1}{\mu}\frac{\partial p}{\partial x} \tag{27}$$

The flux is

$$f_x = \frac{1}{\pi R^2} \int_0^{2\pi} \int_0^R v_x \, dr \, r d\theta = -\frac{1}{8} \frac{1}{\mu} \frac{\partial p}{\partial x} R^2 \left(1 + 4\frac{G}{R}\right) \tag{28}$$

The additional term $4GR$ on the right-hand side of the last equation describes the permeability enhancement by slippage in a cylindrical capillary.

2.3.3. *Example: slippage flow in a rectangular capillary.* In steady flow, the pressure gradient is constant and is aligned with the pipe. The flow lines are parallel to the pipe axis and, as well as the vector of of velocity. Let us denote the magnitude of velocity by v and consider a Cartesian coordinate system whose z axis coincides with one of the edges of the pipe. Then, the Navier–Stokes equations reduce to

$$\frac{\partial^2 v}{\partial x^2} + \frac{\partial^2 v}{\partial y^2} = \frac{1}{\mu} \frac{\partial p}{\partial z} \tag{29}$$

Let a and b be the dimensions of the pipe cross-section, so that $0 \leq x \leq a$ and $0 \leq y \leq b$. The slippage boundary conditions take on the form:

$$v - G\frac{\partial v}{\partial x}\bigg|_{x=0} = 0 \qquad\qquad v + G\frac{\partial v}{\partial x}\bigg|_{x=a} = 0 \tag{30}$$

$$v - G\frac{\partial v}{\partial y}\bigg|_{y=0} = 0 \qquad\qquad v + G\frac{\partial v}{\partial y}\bigg|_{y=b} = 0 \tag{31}$$

The sign change is due to the normal vector orientation, *cf* Equation (18).

Let us seek a solution in the form $v = v_0 + w$, where v_0 is some solution of the Poisson equation (29). Then, w is a solution to the Laplace equation

$$\frac{\partial^2 w}{\partial x^2} + \frac{\partial^2 w}{\partial y^2} = 0 \tag{32}$$

satisfying the boundary conditions:

$$w - G\frac{\partial w}{\partial x}\bigg|_{x=0} = -v_0 + G\frac{\partial v_0}{\partial x}\bigg|_{x=0} \qquad w + G\frac{\partial w}{\partial x}\bigg|_{x=a} = -v_0 - G\frac{\partial v_0}{\partial x}\bigg|_{x=a} \tag{33}$$

$$w - G\frac{\partial w}{\partial y}\bigg|_{y=0} = -v_0 + G\frac{\partial v_0}{\partial y}\bigg|_{y=0} \qquad w + G\frac{\partial w}{\partial y}\bigg|_{y=b} = -v_0 - G\frac{\partial v_0}{\partial y}\bigg|_{y=b} \tag{34}$$

Let us put

$$v_0 = \frac{1}{2\mu} \frac{\partial p}{\partial z} (y^2 - by - Gb) \tag{35}$$

so that the function v_0 does not depend on x and satisfies the boundary conditions (31). Then, Equations (33)–(34) take on the form

$$w - G\frac{\partial w}{\partial x}\bigg|_{x=0} = -v_0 \qquad\qquad w + G\frac{\partial w}{\partial x}\bigg|_{x=a} = -v_0 \tag{36}$$

$$w - G\frac{\partial w}{\partial y}\bigg|_{y=0} = 0 \qquad\qquad w + G\frac{\partial w}{\partial y}\bigg|_{y=b} = 0 \tag{37}$$

Put $w(x, y) = X(x)Y(y)$. then, a standard argument leads to two pairs of solution depending on two parameters

$$X_{\lambda,\alpha}(x) = \cosh(\lambda x + \alpha) \qquad\qquad Y_{\lambda,\gamma}(y) = \cos(\lambda y + \gamma) \tag{38}$$

$$X_{\lambda,\alpha}(x) = \cos(\lambda x + \alpha) \qquad\qquad Y_{\lambda,\gamma}(y) = \cosh(\lambda y + \gamma) \tag{39}$$

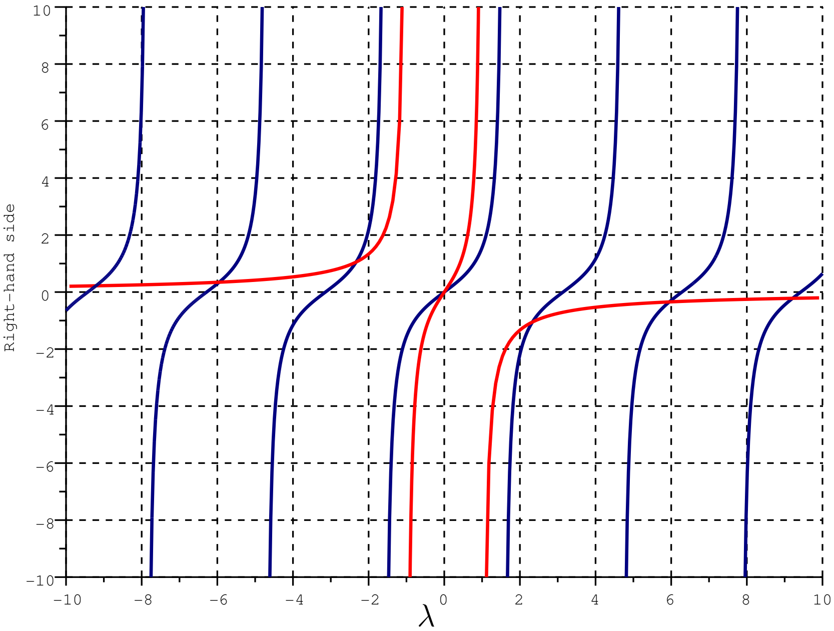

FIGURE 1. The solutions to Equation (43) for $G = 1$ and $b = 1$.

From Equations (37), one obtains two systems of equations to determine λ and γ:

$$\begin{cases} \cos\gamma + G\lambda\sin\gamma & = 0 \\ \cos(\lambda b + \gamma) - G\lambda\sin(\lambda b + \gamma) & = 0 \end{cases} \tag{40}$$

and

$$\begin{cases} \cosh\gamma - G\lambda\sinh\gamma & = 0 \\ \cosh(\lambda b + \gamma) + G\lambda\sinh(\lambda b + \gamma) & = 0 \end{cases} \tag{41}$$

Let us first consider the system of equations (40). It can be rewritten in a simpler form:

$$\begin{cases} \tan\gamma & + \dfrac{1}{G\lambda} = 0 \\ \tan(\lambda b) + \tan\gamma & - \dfrac{1}{G\lambda}\left(1 - \tan(\lambda b)\tan\gamma\right) = 0 \end{cases} \tag{42}$$

Elimination of $\tan\gamma$ yields a transcendent equation with respect to λ:

$$\tan\lambda b = \frac{2G\lambda}{1 - G^2\lambda^2} \tag{43}$$

The plot of the right-hand side of the last equation has two vertical asymptotes, $\lambda = \pm G^{-1}$, and the abscissa is a horizontal asymptote. The solutions to Equation (43) are the λ coordinates of the intersection between the curves shown in Figure 1. The corresponding values of γ are given by $\gamma = \dfrac{\pi}{2} + \arctan(G\lambda)$.

It suffices to find only the positive solutions to Equation (43). Denote by $0 < \lambda_1 < \lambda_2 < \ldots$ the ordered sequence of all solutions, and let γ_n be the sequence of respective gammas. Let us demonstrate that the system of functions

$$Y_n(y) = \cos(\lambda_n y + \gamma_n) \tag{44}$$

in an orthogonal in L_2. Indeed, let $n > m$. Then,

$$\begin{aligned}
&\int_0^b \cos(\lambda_n y + \gamma_n)\cos(\lambda_m y + \gamma_m)\,dy \\
&= \frac{1}{2}\int_0^b \left[\cos((\lambda_n + \lambda_m)y + \gamma_n + \gamma_m) + \cos((\lambda_n - \lambda_m)y + \gamma_n - \gamma_m)\right]\,dy \\
&= \frac{1}{(\lambda_n + \lambda_m)(\lambda_n - \lambda_m)}\Big[(\lambda_n - \lambda_m)\sin((\lambda_n + \lambda_m)y + \gamma_n + \gamma_m)\big|_{y=0}^{y=b} \\
&\quad + (\lambda_n + \lambda_m)\sin((\lambda_n - \lambda_m)y + \gamma_n - \gamma_m)\big|_{y=0}^{y=b}\Big]
\end{aligned} \tag{45}$$

Let us demonstrate that the expression between the square brackets vanishes at $y = 0$ and $y = b$. Put $y = 0$ (the case $y = b$ is analogous):

$$\begin{aligned}
&(\lambda_n - \lambda_m)\sin(\gamma_n + \gamma_m) + (\lambda_n + \lambda_m)\sin(\gamma_n - \gamma_m) \\
&= \lambda_n[\sin(\gamma_n + \gamma_m) + \sin(\gamma_n - \gamma_m)] + \lambda_m[\sin(\gamma_n - \gamma_m) - \sin(\gamma_n + \gamma_m)] \\
&= 2\sin\gamma_n\cos\gamma_m - \frac{2}{G}\cos\gamma_n\cos\gamma_m + \frac{2}{G}\cos\gamma_n\cos\gamma_m - 2\cos\gamma_n\sin\gamma_m \\
&= -\frac{2}{G}\cos\gamma_m(\cos\gamma_n - G\sin\gamma_n) + \frac{2}{G}\cos\gamma_n(\cos\gamma_m - G\sin\gamma_m)
\end{aligned} \tag{46}$$

The expressions between the braces vanish due to the boundary condition. Thus, the system of functions $Y_n(y)$ normalized by $\sqrt{\frac{2}{b}}$ is an orthonormal basis in $L_2([0, b])$. Put

$$C_n = \sqrt{\frac{2}{b}}\int_0^b v_0(y)\cos(\lambda_n y + \gamma_n)\,dy \tag{47}$$

and

$$w = \sum_{n=1}^{\infty} B_n\cosh(\lambda_n x + \alpha_n)\cos(\lambda_n y + \gamma_n) \tag{48}$$

where B_n and α_n must yet to be determined from the boundary conditions. For each n, from Equations (36) one obtains:

$$\begin{aligned}
B_n\cosh(\alpha_n) - GB_n\sinh(\alpha_n) &= -C_n \\
B_n\cosh(\lambda_n a + \alpha_n) + GB_n\sinh(\lambda_n a + \alpha_n) &= -C_n
\end{aligned} \tag{49}$$

Solving the last system of equations for B_n and α_n finalized the solution (48). Dividing the first equation by the second eliminates B_n:

$$\cosh(\alpha_n) - G\sinh(\alpha_n) = \cosh(\lambda_n a + \alpha_n) + G\sinh(\lambda_n a + \alpha_n) \tag{50}$$

Equivalently,

$$\begin{aligned}
\cosh(\alpha_n) - G\sinh(\alpha_n) &= \cosh(\lambda_n a)\cosh\alpha_n + \sinh(\lambda_n a)\sinh\alpha_n \\
&\quad + G\left[\sinh(\lambda_n a)\cosh\alpha_n + \cosh(\lambda_n a)\sinh\alpha_n\right]
\end{aligned} \tag{51}$$

Finally,

$$\tanh\alpha_n = \frac{1 - \cosh(\lambda_n a) - G\sinh(\lambda_n a)}{G + \sinh(\lambda_n a) + G\cosh(\lambda_n a)} \tag{52}$$

and

$$B_n = \frac{C_n}{G\sinh(\lambda_n a) - \cosh(\lambda_n a)} \tag{53}$$

3. A DISCRETIZATION OF THE STOKES EQUATIONS

We employ an iterative procedure of solving (2) and (9), which is implicit in pressures and explicit in velocities. This choice is based primarily on the simplicity of calculations. The idea is based on the projection method [13].

The procedure follows the following scheme. Given v^n and p^n, find v^{n+1} and p^{n+1} by solving the system of equations

$$\nabla \cdot v^{n+1} = 0 \tag{54}$$

$$\frac{v^{n+1} - v^n}{\tau_n} = \eta \nabla^2 v^n - \nabla p^{n+1} \tag{55}$$

The iteration parameter τ_n controls has the dimensionality of time. It can be linked to the Navier-Stokes equations, where both the body force and the nonlinear with respect to the velocity term are neglected. Thus, the iterative numerical solution of steady-state Stokes equations using Equations (55) is equivalent to solving transient equations. Stabilization of the transient solution on a large time interval is equivalent to convergence.

To solve equations (54)–(55) numerically, on each iteration, we formally introduce an auxiliary velocity v^*:

$$\frac{v^{n+1} - v^* + v^* - v^n}{\tau_n} = \eta \nabla^2 v^n + \nabla p^{n+1} \tag{56}$$

Let us require that

$$\frac{v^* - v^n}{\tau_n} = \eta \nabla^2 v^n \tag{57}$$

and

$$\frac{v^{n+1} - v^*}{\tau_n} = \nabla p^{n+1} \tag{58}$$

Thus, v^* can be computed for a given v^n using Equation (57). The computation of v^{n+1} is performed in two steps. Since we require that $\nabla v = 0$ at all iterations, application of divergence to Equation (58) yields

$$\nabla^2 p^{n+1} = -\frac{1}{\tau_n} \nabla \cdot v^* \tag{59}$$

The latter is a Poisson equation for p^{n+1}. Once this equations is solved, v^{n+1} is computed from Eq. (58). Clearly, since v^* and p^{n+1} satisfy Equation (58), the next velocity iteration, v^{n+1}, is divergence-free. The iterations are stopped if the increment in pressures or velocities becomes smaller some tolerance value. Due to the linearity of the problem, it can be solved only for a certain set of normalized boundary conditions and then the solution can be rescaled as needed.

The discretized computational domain can be naturally derived from the rectangular Cartesian structure of a 3D micro-tomography image. The marker-and-cell method (MAC), see [28], can be used for discretization of divergence, gradient and Laplace operator. Discretization of the latter requires to numerically approximate the second-order partial derivatives $\partial^2 v/\partial x^2$, $\partial^2 v/\partial y^2$, and $\partial^2 v/\partial z^2$, which is considered below. In a MAC discretization, pressures are evaluated at the voxel centers, whereas the velocities are evaluated at the centers of the square interfaces separating neighbor voxels, see Figure 2. Note that only the scalar products of the velocity and normal vectors are involved in computations. As a consequence, there is no such a grid location where all three components of velocity need to be evaluated simultaneously.

Let i, j and k characterize the position of a voxel in the image. We evaluate the pressures at the voxel centers. For the second-order derivatives, we use standard discretization scheme. For

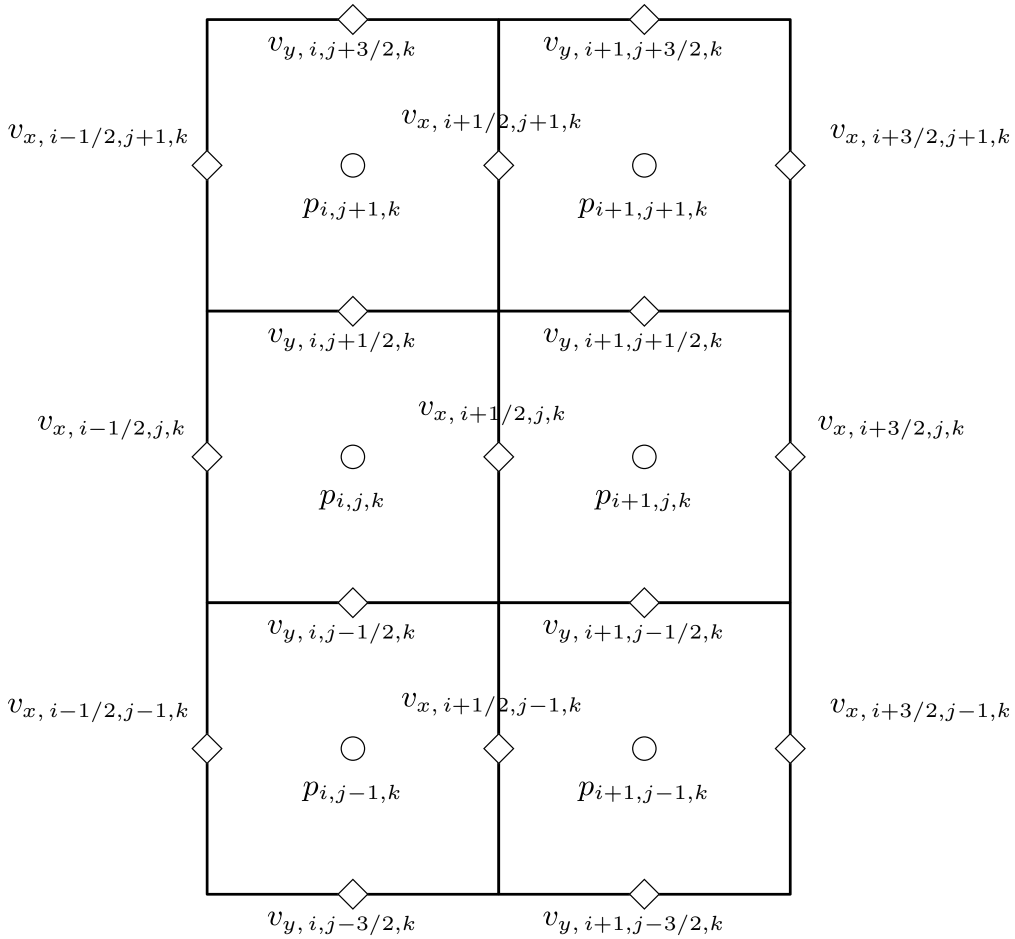

FIGURE 2. The circles mark the voxel centers, where the pressures are evaluated. The triangles mark the centers of the interfaces between voxels, where the velocities are evaluated. This is a 2D slice of a 3D grid, so index k is the same for all voxels.

example,

$$\left.\frac{\partial^2 v_x}{\partial x^2}\right|_{x=x_{i+1/2,j,k}} = \frac{v_{x,\,i-1/2,j,k} - 2v_{x,\,i+1/2,j,k} + v_{x,\,i+3/2,j,k}}{d^2} + O(d^2) \tag{60}$$

and

$$\left.\frac{\partial^2 v_x}{\partial y^2}\right|_{x=x_{i+1/2,j,k}} = \frac{v_{x,\,i+1/2,j-1,k} - 2v_{x,\,i+1/2,j,k} + v_{x,\,i+1/2,j+1,k}}{d^2} + O(d^2) \tag{61}$$

where d is the voxel size.

With second derivative defined like in Eq. (60)–(61), the Laplace operator is numerically evaluation is linked to $x = x_{i+1/2,j,k}$. This location is consistent with the numerical evaluation of the pressure gradient components:

$$\left.\frac{\partial p}{\partial x}\right|_{x=x_{i+1/2,j,k}} = \frac{p_{i+1,j,k} - p_{i,j,k}}{d} + O(d^2) \tag{62}$$

Hence, the discretisation is consistent with Eq. (9) with a second-order accuracy.

4. BOUNDARY CONDITIONS

In this section, we consider two types of boundary conditions: the conditions at the pore walls, and the conditions at the inlet and outlet boundaries of the sample.

4.1. **Pore walls.** First, let us discretise the no-slip boundary conditions at the pore walls. We will have to consider all possible combinations of the solid and pore neighbor voxels in the stencil. In stencil figures in this subsection, the solid voxels are shaded, whereas pore voxels are blanc. The central node of the stencil (index i) is labeled by a filled triangle.

Note that there are two types of partial derivatives of the components of velocity vector: the derivative in the direction of the component, and the derivatives in the orthogonal directions. Let us consider derivatives of v_y in x. The derivatives of v_z in x, v_x in y, *etc.*can done in a similar way. To shorten the notations, the indices j and k, as well as the subscripts x, y, and z are dropped whenever it does not lead to a confusion.

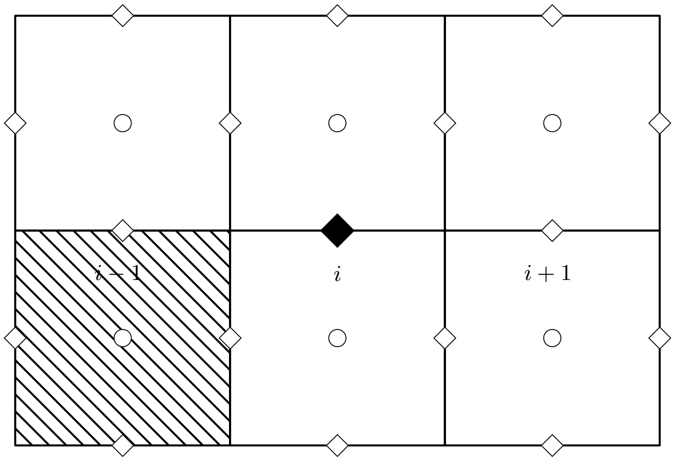

FIGURE 3. One solid voxel at $i-1, j, k$ or $i-1, j+1, k$

In a configuration shown in Fig. 3 one and only one voxel is in the solid phase. The no-slip condition, $v_{i-1} = 0$, reduces Eq. (60) to

$$\left.\frac{\partial^2 v}{\partial x^2}\right|_{x=x_i} \sim -2v_i + v_{i+1} \tag{63}$$

This equation approximates the second-order partial derivative at the point marhewd by filled diamond in Figure 3. Similarly, if the solid-pore inter-voxel boundary were at $i = i+1$, but not at $i = i-1$, then one would obtain

$$\left.\frac{\partial^2 v}{\partial x^2}\right|_{x=x_i} \sim v_{i-1} - 2v_i \tag{64}$$

If exactly two solid voxels located on both sides of voxel i, for instance, like in Figure 4, then the discretization of the second order partial derivative is further simplified:

$$\left.\frac{\partial^2 v}{\partial x^2}\right|_{x=x_i} \sim -2v_i \tag{65}$$

A slightly more complex situation is in a case where two solid voxels are next to each other, Fig. 5. In such a case, the no-slip condition is formulated at the interface $i-1/2$. Let us introduce a “ghost” velocity at solid voxel $i-1$. Since

$$v_{i-1/2} = \frac{v_{i-1} + v_i}{2} + O(d^2) \tag{66}$$

the boundary condition can be discretized as

$$\frac{v_{i-1} + v_i}{2} = 0 \tag{67}$$

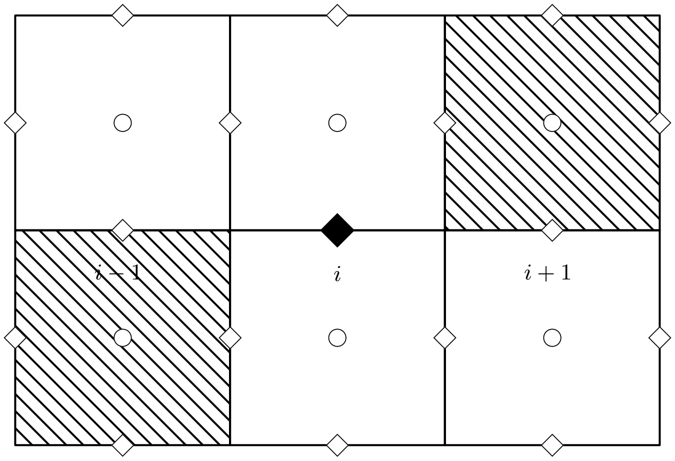

FIGURE 4. Two solid voxels at $i-1, j, k$ and $i+1, j+1, k$

Hence, for the second derivative, one obtains

$$\left.\frac{\partial^2 v}{\partial x^2}\right|_{x=x_i} \sim -3v_i + v_{i+1} \tag{68}$$

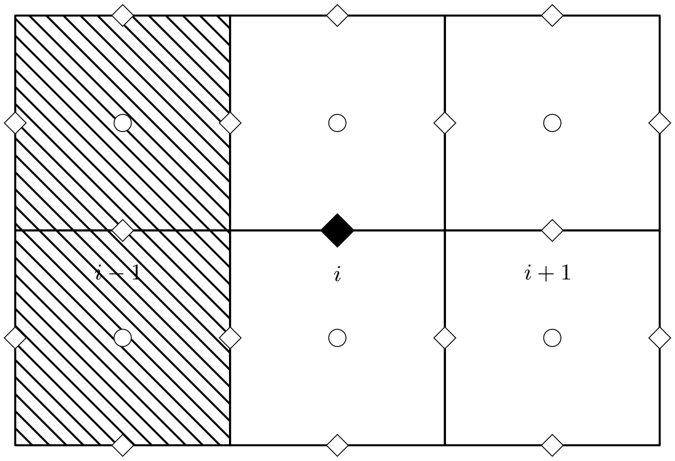

FIGURE 5. Two solid voxels at $i-1, j, k$ and $i-1, j+1, k$

If, in addition, exactly one of voxels with index $i+1$ is solid, for example, like in Fig. 6, then the no-slip boundary condition implies that

$$\left.\frac{\partial^2 v}{\partial x^2}\right|_{x=x_i} \sim -3v_i \tag{69}$$

If both voxels, $i+1, j, k$ and $i+1, j+1, k$ are in solid phase, Figure 7, then no-slip condition is approximated by Equation (67). Thus, in such a a one-voxel wide channel,

$$\left.\frac{\partial^2 v}{\partial x^2}\right|_{x=x_i} \sim -4v_i \tag{70}$$

Figures 8 9 show the only two stencil configurations involving boundary conditions for the velocity component derivatives in the component direction. In the first case,

$$\left.\frac{\partial^2 v}{\partial x^2}\right|_{x=x_{i+1/2}} \sim -2v_{i+1/2} + v_{i+3/2} \tag{71}$$

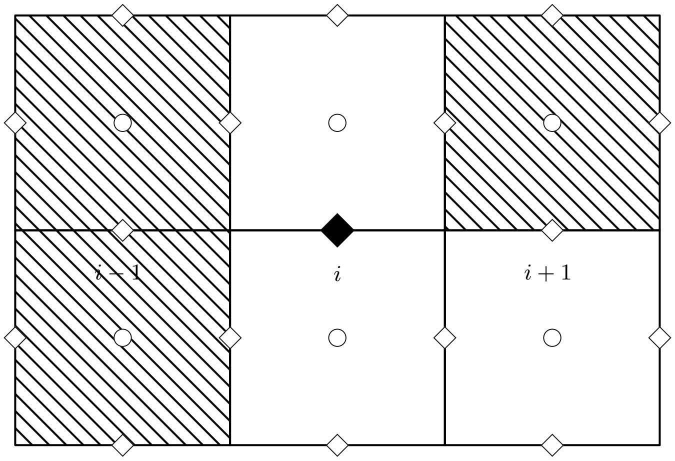

FIGURE 6. Three solid voxels at $i-1,j,k$, $i-1,j+1,k$, and $i+1,j+1,k$

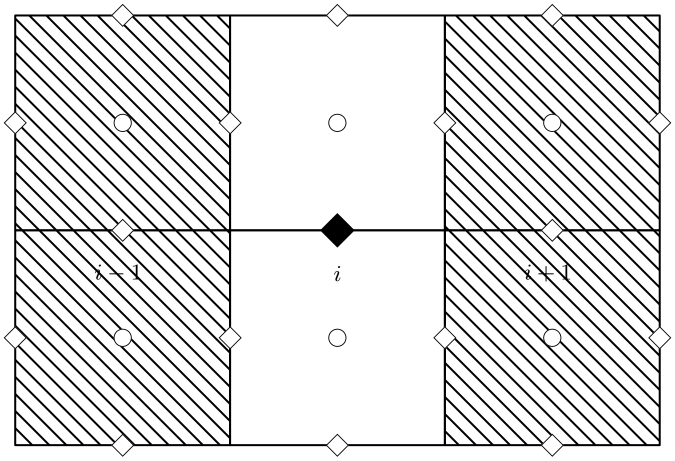

FIGURE 7. Four solid voxels at $i-1,j,k$, $i-1,j+1,k$, $i+1,j,k$, and $i+1,j+1,k$

whereas in the second one,

$$\left.\frac{\partial^2 v}{\partial x^2}\right|_{x=x_{i+1/2}} \sim -2v_{i+1/2} \tag{72}$$

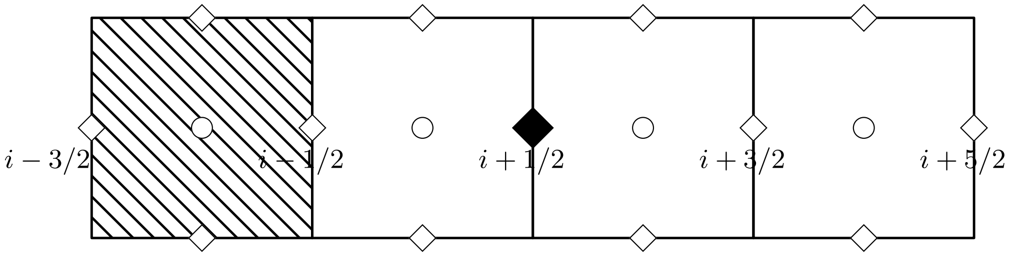

FIGURE 8. Interaction with no-slip condition at the wall for $\dfrac{\partial^2 u_x}{\partial x^2}$, $\dfrac{\partial^2 u_y}{\partial y^2}$, and $\dfrac{\partial^2 u_z}{\partial z^2}$.

For pressures, at a wall orthogonal to x axis, from Equation (9) one infers that

$$\left.\frac{\partial p}{\partial x}\right|_{\text{Wall}} = \eta \left.\frac{\partial^2 v_x}{\partial x^2}\right|_{\text{Wall}} \tag{73}$$

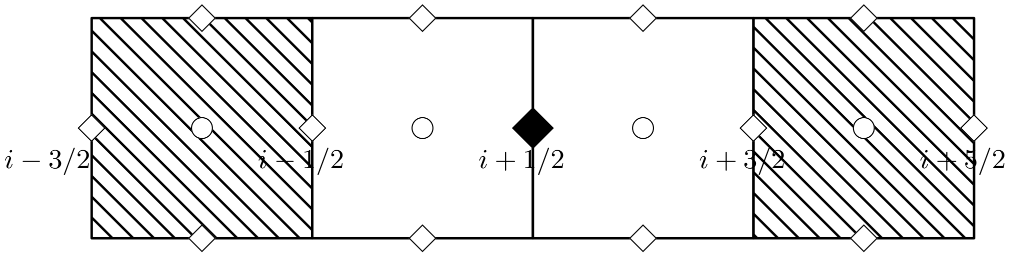

FIGURE 9. Interaction with no-slip condition at the wall for $\dfrac{\partial^2 u_x}{\partial x^2}$, $\dfrac{\partial^2 u_y}{\partial y^2}$, and $\dfrac{\partial^2 u_z}{\partial z^2}$.

In [42] the boundary condition (73) was replaced by zero normal derivative of the pressures at the walls:

$$\left.\frac{\partial p}{\partial n}\right|_{\text{Wall}} = 0 \tag{74}$$

This discretization was erroneously explained as an implication of Stokes equations. Indeed, condition (74) holds true in Poiseuille-type flow in a pipe. However it is incorrect, for example, in creeping flow around a sphere [39]. In flow in the pore space of a natural rock, whose geometry is usually extremely complex, there is no justification for adopting Equation (74).

Figures 10–12 show all possible configurations for a wall orthogonal to x axis For a configuration in Figure 10, one puts

$$\left.\frac{\partial^2 p}{\partial x^2}\right|_{i,j,k} \sim \frac{\dfrac{p_{i+1,j,k} - p_{i,j,k}}{d} - \eta \dfrac{\partial^2 v^x_{i-1/2,j,k}}{\partial x^2}}{d} \tag{75}$$

Similarly, for a configuration in Figure 11, one obtains

$$\left.\frac{\partial^2 p}{\partial x^2}\right|_{i,j,k} \sim \frac{\eta \dfrac{\partial^2 v^x_{i+1/2,j,k}}{\partial x^2} - \dfrac{p_{i,j,k} - p_{i-1,j,k}}{d}}{d} \tag{76}$$

For consistency, the second derivative of the velocity should be approximated with at least a second degree of accuracy. Both, the velocity v_x and its first derivatives with respect to y and z vanish at the wall. Incompressibility condition (2) implies that

$$\frac{\partial v_x(x_{i-1/2})}{\partial x} = 0 \tag{77}$$

as well. Hence, using Taylor series, we obtain

$$v^x_{i+1/2,j,k} = \frac{\partial^2 v^x_{i-1/2,j,k}}{\partial x^2}\frac{d^2}{2} + \frac{\partial^3 v^x_{i-1/2,j,k}}{\partial x^3}\frac{d^3}{6} + O(d^4) \tag{78}$$

and

$$v^x_{i+3/2,j,k} = \frac{\partial^2 v^x_{i-1/2,j,k}}{\partial x^2}\frac{4d^2}{2} + \frac{\partial^3 v^x_{i-1/2,j,k}}{\partial x^3}\frac{8d^3}{6} + O(d^4) \tag{79}$$

Thus, combining Equations (78) and (79),

$$\frac{\partial^2 v^x_{i-1/2,j,k}}{\partial x^2} = \frac{8v^x_{i+1/2,j,k} - v^x_{i+3/2,j,k}}{2d^2} + O(d^2) \tag{80}$$

Similarly, if the voxel $i-2,j,k$ is in pore space, for a configuration in Figure 11,

$$\frac{\partial^2 v^x_{i+1/2,j,k}}{\partial x^2} = \frac{8v^x_{i-1/2,j,k} - v^x_{i-3/2,j,k}}{2d^2} + O(d^2) \tag{81}$$

If the voxel $i-2, j, k$ is solid, then the term $v^x_{i-3/2,\,j,k}$ in the last equation must be replaced by zero.

Consequently, or a configuration in Fig. 10, one gets

$$\left.\frac{\partial^2 p}{\partial x^2}\right|_{i,j,k} \sim \frac{p_{i+1,\,j,k} - p_{i,\,j,k} - \eta \dfrac{8v^x_{i+1/2,\,j,k} - v^x_{i+3/2,\,j,k}}{2d}}{d^2} \tag{82}$$

fSimilarly, for a configuration in Fig. 11,

$$\left.\frac{\partial^2 p}{\partial x^2}\right|_{i,j,k} \sim \frac{\eta \dfrac{8v^x_{i-1/2,\,j,k} - v^x_{i-3/2,\,j,k}}{2d} - (p_{i-1,\,j,k} - p_{i,\,j,k})}{d^2} \tag{83}$$

Again, if the voxel $i-2, j, k$ is solid, then the term $v^x_{i-3/2,\,j,k}$ in the last equation must be replaced by zero. Note that the accuracy of the last two equations is only of the first order.

For a configuration in Figure 12, the second pressure derivative is approximately equal to zero:

$$\left.\frac{\partial^2 p}{\partial x^2}\right|_{i,\,j,k} \sim 0 \tag{84}$$

This configuration describes flow through a narrow channel, therefore Poiseuille-type conditions are applicable.

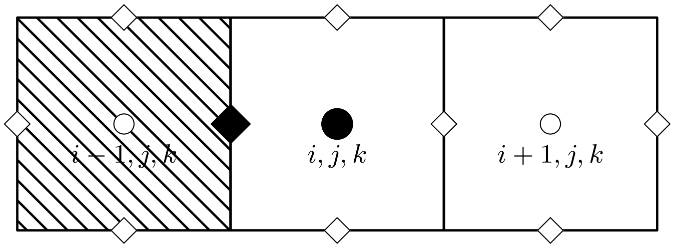

FIGURE 10. Interaction with no-slip condition at the wall for pressure: the filled circle marks the center of the stencil, and the filled diamond marks the point where the pressure normal derivative is approximated.

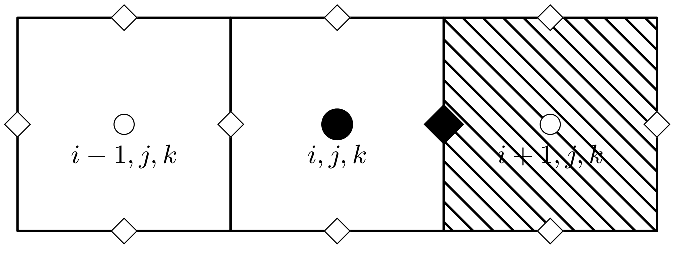

FIGURE 11. Interaction with no-slip condition at the wall for pressures: a one-voxel-wide channel between two walls and a corner. The filled circle marks the center of the stencil, and the filled diamond marks the point where the pressure normal derivative is approximated.

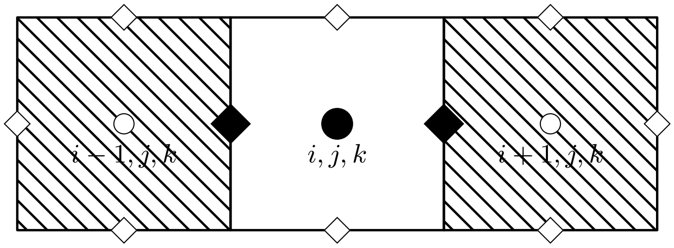

FIGURE 12. Interaction with no-slip condition at the wall for pressures: a one-voxel-wide channel between two walls and a corner. The filled circle marks the center of the stencil, and the filled diamonds mark the points where the pressure normal derivative is approximated.

4.2. **Discretization of the slippage boundary condition.** Discretization of the slippage boundary condition, Equation (16), must be centered at the wall. If the wall boundary is associated with the center of a grid cell, the no-slip conditions must be formulated at this center. For example, consider the velocity component v_x at a wall boundary orthogonal to y. A second-order finite-difference approximation is furnished by the following formula:

$$v_x - G\frac{\partial v_x}{\partial n}\bigg|_{i,j,k} = \frac{v_{x,i,j+1,k}+v_{x,i,j,k}}{2} - G\frac{v_{x,i,j+1,k}-v_{x,i,j,k}}{h} + O(h^2) \tag{85}$$

Thus,

$$v_{x,\,i,j,k} = \frac{\dfrac{1}{2}-\dfrac{G}{h}}{\dfrac{1}{2}+\dfrac{G}{h}} v_{x,\,i,j+1,k} = \frac{h-2G}{h+2G} v_{x,\,i,j+1,k} \tag{86}$$

Let voxel (i,j,k) be a pore voxels, but both voxels $(i,j+1,k)$ and $(i+1,j+1,k)$ be solid. In such a case, the velocity v_x is parallel to the wall and the slip condition, Equation (16), applies. Let us formally introduce velocity v_x for the voxel $(i,j+1,k)$. Then, at the boundary, the slip condition yields

$$\frac{v_{x,\,i,j+1,k}+v_{x,\,i,j,k}}{2} = -G\frac{v_{x,\,i,j+1,k}-v_{x,\,i,j,k}}{h} \tag{87}$$

The last equation approximates the the Maxwell slip boundary condition, Equation (16), to the second order accuracy, $O(d^2)$. The minus sign on the right-hand side is because the normal is directed against the axis y. Thus,

$$v_{x,\,i,j+1,k} = \frac{2G-h}{2G+h} v_{x,\,i,j+1,k} \tag{88}$$

Similarly, if the voxel (i,j,k) is pore, but both $(i,j-1,k)$ and $(i+1,j-1,k)$ are solid, then the discretized slip condition is

$$\frac{v_{x,\,i,j,k}+v_{x,\,i,j-1,k}}{2} = G\frac{v_{x,\,i,j,k}-v_{x,\,i,j-1,k}}{h} \tag{89}$$

In this case, the normal and the axis y are co-directed, so the sign is plus. Thus,

$$v_{x,\,i,j-1,k} = \frac{2G-h}{2G+h} v_{x,\,i,j,k} \tag{90}$$

If $G=0$, the fraction on the right hand sides of Equation (89), reduce to -1, so that on the boundary the velocity is zero, which is the no-slip condition.

4.3. **Image boundaries.** The permeability tensor can be estimated by running flow simulations three times with three different Dirichlet boundary conditions for the pressures. Each time, a pair of opposite faces of the three-dimensional image are called inlet and outlet and pressure values p_{in} and p_{out} are assigned. Due to the linearity, the values p_{in} and p_{out} can be assigned arbitrarily, for example, $p_{\text{in}} = N - 1$ and $p_{\text{out}} = 0$, where N is the size of the domain in voxels. The velocity and pressure in physical units can be obtained after the solution is found, see Section 4.6 below.

Consider the following boundary condition for for velocities:

$$\beta \frac{\partial v}{\partial n} + v = 0 \tag{91}$$

This general condition does not close the boundaries for flow, both in normal and lateral directions. To mimic a sleeve around the core, a layer of solid voxels can be added in the direcations orthogonal to the flow. Adding such a layer makes the boundary condition defined in Equation (91) irrelevant.

The pressures at the inlet at outlet faces, are given by Dirichlet boundary conditions mentioned above. Hence, the Poisson equation for pressures, Equation (59), us solved only at the interior voxels of the image. The right-hand side of this equation is evaluated straightforwardly since in MAC scheme the normal components of velocity v^* are evaluated at the voxel boundaries.

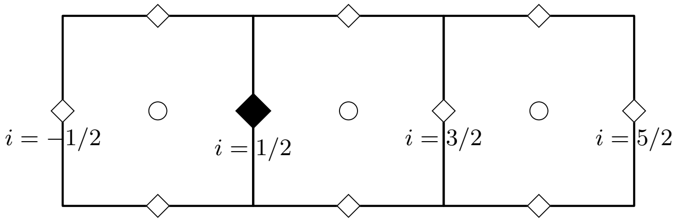

FIGURE 13. Velocity discretization at the boundary: the voxels between $i = -1/2$ and $i = 1/2$ is at the boundary.

Updating velocities at each iteration requires an evaluation of the Laplacian, see Equation (57). The latter can be done by introduction of ghost velocity values at the next-to-boundary faces of the boundary pore voxels. These ghost values are then eliminated using the boundary conditions (91). The boundary condition for velocities are formulated at the voxel faces next to the actual boundary of the image. For example, Figure 13 shows a typical voxels configuration. For velocity component v_x, the boundary condition defined by Equations (91) will be attached to the point $i = 1/2$. A second order approximation is provided by

$$-\frac{1}{2}\beta(v^x_{3/2} - v^x_{-1/2}) + v^x_{1/2} = 0 \tag{92}$$

or

$$v^x_{-1/2} = v^x_{3/2} - \frac{2}{\beta} v^x_{1/2} = 0 \tag{93}$$

A substitution into Equation (60) yields

$$\left.\frac{\partial^2 v^x}{\partial x^2}\right|_{i=1/2} \sim -2\left(1 + \frac{1}{\beta}\right) v^x_{1/2} + 2v^x_{3/2} \tag{94}$$

The last equation remains valid whether $i = 3/2$ is at the pore wall or not.

Figure 14 shows a typical configuration for the other components of velocity. A second-order approximation of the boundary condition is provided by

$$-\beta(v^y_1 - v^y_0) + \frac{1}{2}(v^y_1 + v^y_0) = 0 \tag{95}$$

or

$$v_0^y = \frac{2\beta - 1}{2\beta + 1} v_1^y \tag{96}$$

Finally, one obtains:

$$\left.\frac{\partial^2 v^y}{\partial x^2}\right|_{i=1} \sim -\frac{2\beta + 3}{2\beta + 1} v_1^y + v_2^y \tag{97}$$

The last formula is valid only if no more than one voxel at $i = 1$ is solid. If both voxels at $i = 1$ are solid (see Figure 15) then Equation (67) has to be applied instead. Thus, for the configuration in Fig. 15,

$$\left.\frac{\partial^2 v_x^y}{\partial x^2}\right|_{i=1} \sim -4\frac{\beta + 1}{2\beta + 1} v_1^y \tag{98}$$

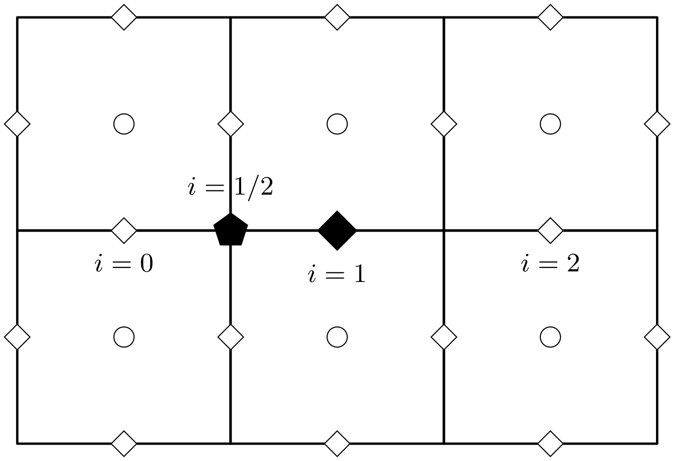

Figure 14. Velocity discretization at the boundary: the filled triangle marks the point where the Laplacian is evaluated and the filled pentagon marks the location where the boundary condition is evaluated.

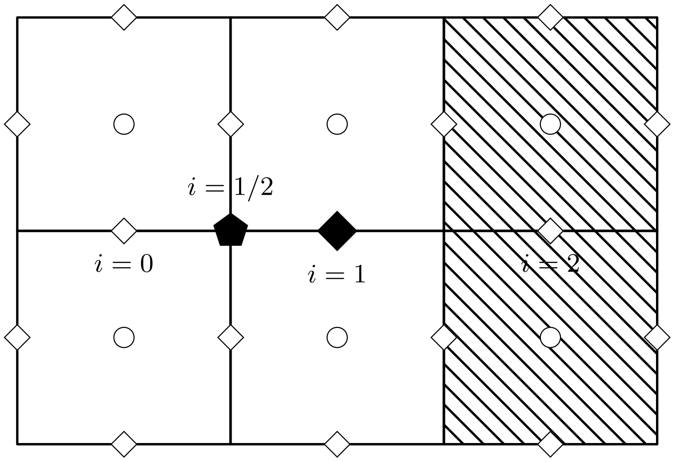

Figure 15. Velocity discretization at the boundary: a pore wall next to the boundary case.

Note that the for corner voxels do not require any special treatment. Also the MAC discretization shifts the boundary for velocities by a half-voxel relative to the boundary for pressures. This is a consequence of the fact that velocities and pressures are evaluated at different points.

Once the formulated boundary problem is solved for three boundary conditions based on

$$\nabla p = \begin{pmatrix} 1 \\ 0 \\ 0 \end{pmatrix}, \begin{pmatrix} 0 \\ 1 \\ 0 \end{pmatrix}, \begin{pmatrix} 0 \\ 0 \\ 1 \end{pmatrix} \tag{99}$$

three average volumetric fluxes, or Darcy velocities can be estimated. These three vectors make the permeability tensor of the respective image.

4.4. **The method of artificial compressibility.** Here we describe an implementation of the method of artificial compressibility proposed by Chorin [12]. The idea of artificial compressibility method is as follows: we replace Navier–Stokes equation (7) with zero-divergence incompressibility condition with a system of equations

$$\frac{\partial}{\partial t}\mathbf{v} + \mathrm{Re}(\mathbf{v} \cdot \nabla)\mathbf{v} = -\nabla p + \nabla^2 \mathbf{v} + \mathcal{F} \tag{100}$$

$$\frac{\partial \rho}{\partial t} + \nabla \cdot \mathbf{v} = 0 \tag{101}$$

The last equations are written in standard dimensionless variables:

$$\mathbf{v}' = \frac{\mathbf{v}}{V}, \quad \mathbf{r}' = \frac{\mathbf{r}}{D}, \quad p' = \frac{Dp}{\varrho_0 \nu V}, \quad \mathcal{F}' = \frac{\nu V}{D^2}\mathcal{F}, \quad t' = \frac{\nu}{D^2}t \tag{102}$$

Parameters V and D characterize typical velocity and distance scales, and $\mathrm{Re} = \dfrac{VD}{\nu}$ is the Reynolds number. We drop the primes for brevity. Here ϱ_0 is the actual density of the fluid, whereas ρ in Equation (101) is an artificial density. The latter is related to the fluid pressure through a simple linear relationship $\rho = \delta p$. This compressibility is introduced for computations only. Although the linear compressibility law resembles that for an ideal gas, in the present context it has no physical meaning. We utilize the assumption of creeping flow, that is, we assume that Reynolds number equals zero: $\mathrm{Re} = 0$. This assumption eliminates the only nonlinear term in the system of equations to solve. We seek a steady solution, so all time derivatives vanish. In particular, Equation (101) transforms into an equation of incompressibility.

4.4.1. *Discretization of Equations* (100)–(101). To discretize equations (100)– (101) we employ DuFort–Frankel pattern, as it has been done in the Chorin's work [12] but on MAC staggered scheme, where the velocities are evaluated on the boundaries of the grid cells, but the densities and pressures are evaluated at the centers.

The grid in our case is rectangular. The computations involve only the normal velocity components evaluated at the cell boundaries. Let $\mathbf{v} = (v_x, v_y, v_z)$. For example, v_x is evaluated only at the centers of the boundaries of the cells, which are orthogonal to the x coordinate axis, Figure 16.

Let N_x, N_y, and N_z be the dimensions of the grid. To enumerate all grid cells, we use zero-based indices $i = 0, 1, \ldots, N_x - 1$, $j = 0, 1, \ldots, N_y - 1$, and $k = 0, 1, \ldots, N_z - 1$. For grid boundaries, we will use indices i_v, j_v, and k_v. The subscript $_v$ indicates that the index is associated with respective velocity component. The number of boundaries orthogonal to each coordinate direction exceeds the corresponding number of cells by one. For example, in Figure 16, the x-boundaries of a cell with the indices i, j, k is bounded in direction x are labelled with indices $i_v = i$, $j_v = j$, $k_v = k$ and $i_v = i + 1$, $j_v = j$, and $k_v = k$.

Since the velocities are evaluated at the centers of the respective cell faces, each velocity coordinate is enumerated with one velocity index and two "regular" cell indices. For example the x-component of the velocity vector is enumerated with indices $i_v = 0, 1, \ldots, N_x$, $j = 0, 1, \ldots, N_y - 1$, and $k = 0, 1, \ldots, N_z - 1$. Figure 17 shows indexation of a cross-section of the grid by a plane orthogonal to z.

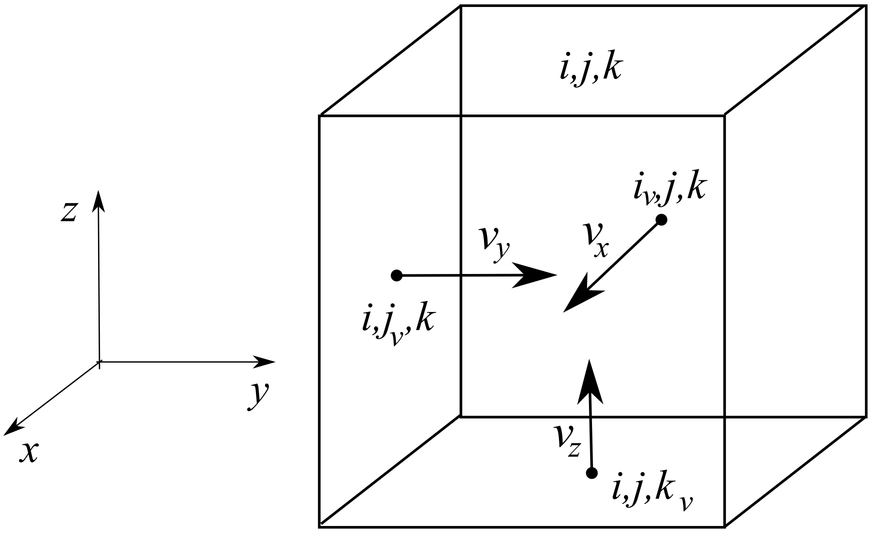

FIGURE 16. Voxel and fluid velocity components enumeration: $i_v = i+1$, $j_v = j+1$, and $k_v = k+1$, where i, j, k are the indices of the voxel center.

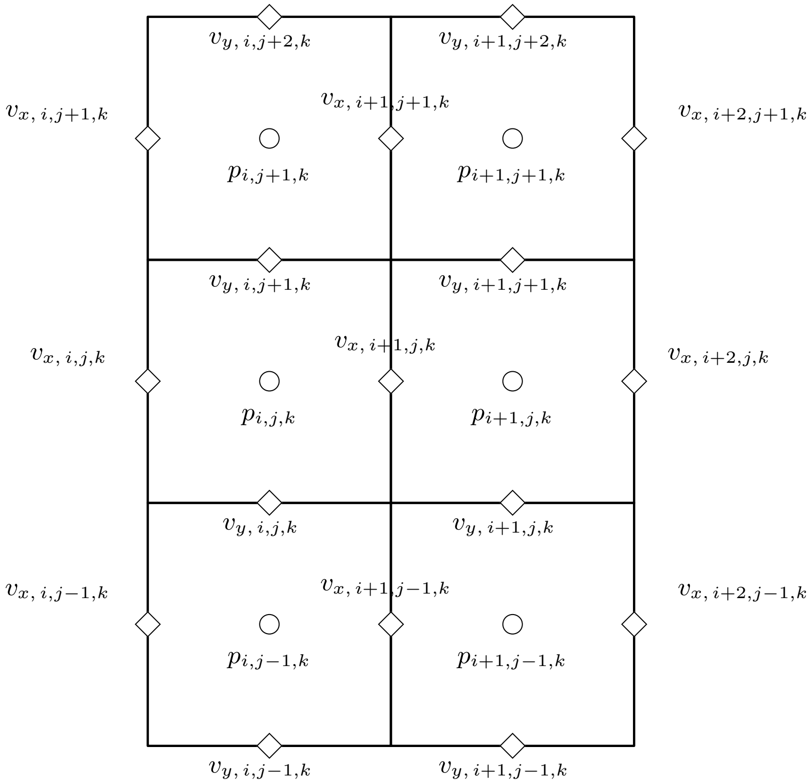

FIGURE 17. The circles mark voxel centers, where the pressures are evaluated. The diamonds mark the centers of the interfaces between voxels, where the velocities are evaluated. This is a 2D slice of a 3D grid in plane x, y.

Let the time variable be discretized with an increment step τ. The enumeration corresponding to the time variable will be denoted by a zero-based superscript ^{n}. Thus, $v^n_{x\,i,j,k}$ denotes the x-component of the velocity evaluated at the center of the "left" wall of the grid cell with indices i, j, k on time step n. Since the pressures and densities are evaluated at the centers of the grid cells, or voxels, their indexation is straightforward, Figure 17.

DuFort–Frankel pattern is a three-layer scheme. Let velocities and pressures have been computed on the time layers $n-1$ and n. The time derivative is evaluated at layer n. The second-order partial derivatives are approximated in the following way:

$$\frac{\partial^2 v_x}{\partial x^2} \approx \frac{(v^n_{x,\,i_v+1,j,k} - v^{n+1}_{x,\,i_v,j,k}) - (v^{n-1}_{x,\,i_v,j,k} - v^n_{x,\,i_v-1,j,k})}{h^2} \tag{103}$$

$$\frac{\partial^2 v_x}{\partial y^2} \approx \frac{(v^n_{x,\,i_v,j+1,k} - v^{n+1}_{x,\,i_v,j,k}) - (v^{n-1}_{x,\,i_v,j,k} - v^n_{x,\,i_v,j-1,k})}{h^2} \tag{104}$$

$$\frac{\partial^2 v_x}{\partial z^2} \approx \frac{(v^n_{x,\,i_v,j,k+1} - v^{n+1}_{x,\,i_v,j,k}) - (v^{n-1}_{x,\,i_v,j,k} - v^n_{x,\,i_v,j,k-1})}{h^2} \tag{105}$$

Here h is the voxel size. Note that the velocity in the center point of the stencil is evaluated on time layers $n-1$ and $n+1$, all other values are from the time layer n. Otherwise, the terms with the plus sign are from layer n, other terms are from layers $n-1$ and $n+1$.

In the center node of a boundary between interior cells $i_v = i+1, j, k$, the respective component of Navier–Stokes equation (100) is approximated by a finite difference equation

$$\begin{aligned}\frac{v^{n+1}_{x,\,i_v,j,k} - v^{n-1}_{x,\,i_v,j,k}}{2\tau} = {} & \frac{v^n_{x,\,i_v-1,j,k} + v^n_{x,\,i_v+1,j,k} - v^{n-1}_{x,\,i_v,j,k} - v^{n+1}_{x,\,i_v,j,k}}{h^2} \\ & + \frac{v^n_{x,\,i_v,j-1,k} + v^n_{x,\,i_v,j+1,k} - v^{n-1}_{x,\,i_v,j,k} - v^{n+1}_{x,\,i_v,j,k}}{h^2} \\ & + \frac{v^n_{x,\,i_v,j,k-1} + v^n_{x,\,i_v,j,k+1} - v^{n-1}_{x,\,i_v,j,k} - v^{n+1}_{x,\,i_v,j,k}}{h^2} + \frac{\rho^n_{i+1,j,k} - \rho^n_{i,j,k}}{\delta h}\end{aligned} \tag{106}$$

Thus,

$$\begin{aligned}v^{n+1}_{x,\,i_v,j,k} = {} & \frac{h^2 - 6\tau}{h^2 + 6\tau} v^{n-1}_{x,\,i_v,j,k} \\ & + \frac{2\tau}{h^2 + 6\tau}\big(v^n_{x,\,i_v-1,j,k} + v^n_{x,\,i_v+1,j,k} + v^n_{x,\,i_v,j-1,k} + v^n_{x,\,i_v,j+1,k} \\ & + v^n_{x,\,i_v,j,k-1} + v^n_{x,\,i_v,j,k+1}\big) + \frac{2\tau h}{\delta(h^2 + 6\tau)}(\rho^n_{i+1,j,k} - \rho^n_{i,j,k})\end{aligned} \tag{107}$$

The artificial compressibility equation (101) is approximated by

$$\frac{\rho^{n+1}_{x,\,i_v,j,k} - \rho^{n-1}_{x,\,i_v,j,k}}{2\tau} = \frac{v^n_{x,\,i_v,j,k} - v^n_{x,\,i_v-1,j,k}}{h} + \frac{v^n_{y,\,i,j_v,k} - v^n_{y,\,i,j_v-1,k}}{h} + \frac{v^n_{z,\,i,j,k_v} - v^n_{z,\,i,j,k_v-1}}{h} \tag{108}$$

Or,

$$\rho^{n+1}_{x,\,i_v,j,k} = \rho^{n-1}_{x,\,i_v,j,k} + \frac{2\tau}{h}\big(v^n_{x,\,i_v,j,k} - v^n_{x,\,i_v-1,j,k} + v^n_{y,\,i,j_v,k} - v^n_{y,\,i,j_v-1,k} + v^n_{z,\,i,j,k_v} - v^n_{z,\,i,j,k_v-1}\big) \tag{109}$$

Here $i_v = i+1$, $j_v = j+1$, and $k_v = k+1$. Note that Equation (106) approximates the first Equation (100) at the center of the cell boundary i_v, j, k, whereas Equation (108) approximates equation (101) in the center of the cell i, j, k.

4.4.2. *Finite difference approximation near the pore walls inside the sample.* When one of the faces of the cells in stencil is at the boundary of the solid, or if one of the cells is in the solid, the scheme described above needs a modification. On the pore walls, we implement no-slip boundary condition by assigning zero velocity. There are several typical situations, which will be addressed below individually.

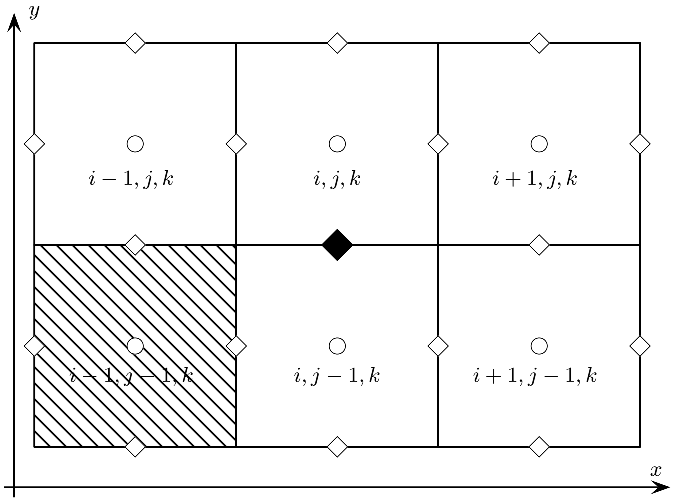

Figure 18. A stencil with a pore wall corner.

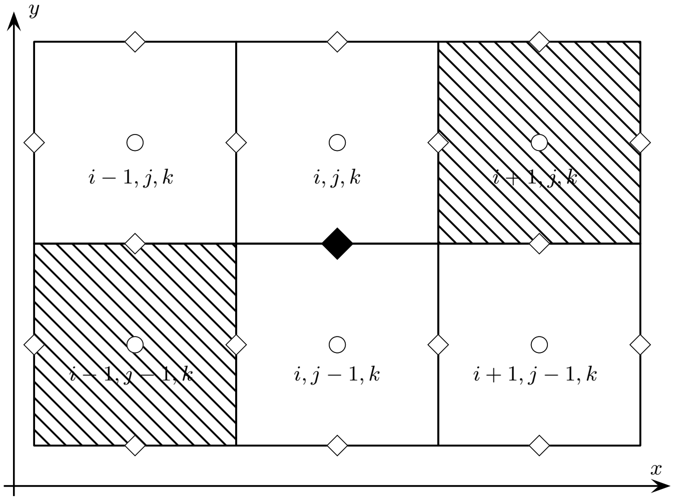

Figure 19. A stencil with two pore wall corners.

For the second-order derivative of v_y in x in a situation like in Figure 18, we simply put

$$\left.\frac{\partial^2 u_y}{\partial x^2}\right|^n_{i,j_v,k} \approx \frac{v^n_{y,i+1,j_v,k} - v^{n-1}_{x,i,j_v,k} - v^{n+1}_{y,i,j_v,k}}{h^2} \tag{110}$$

Similar configuration in other coordinate components are handled similarly. For example, in a situation shown in Figure 19, one obtains

$$\left.\frac{\partial^2 u_y}{\partial x^2}\right|^n_{i,j_v,k} \approx \frac{-v^{n-1}_{x,i,j_v,k} - v^{n+1}_{y,i,j_v,k}}{h^2} \tag{111}$$

In both cases, $j_v = j+1$.

If the stencil encounters a wall, like it is shown in Figure 20, the zero-flow boundary condition must be formulated at the midpoint between points $i-1, j_v, k$ and i, j_v, k. The node $i-1, j_v, k$ is outside the pore space, so we use it as a ghost node and assign v_y be equal to $-v^n_{y\,i,j_v,k}$. Thus, the

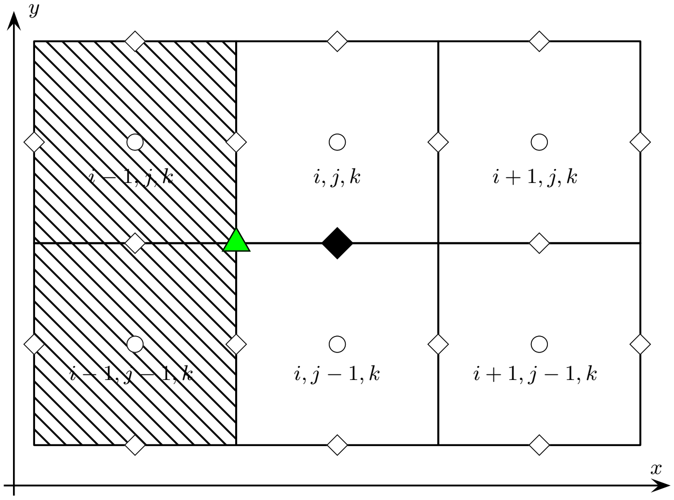

FIGURE 20. A stencil encountering a pore wall. The center is shown as a black filled diamond.

approximation of the second derivative in x takes on the form:

$$\left.\frac{\partial^2 u_y}{\partial x^2}\right|_{i,j_v,k}^{n} \approx \frac{v^n_{y,\,i+1,j_v,k} - v^n_{y,\,i,j_v,k} - v^{n+1}_{y,\,i,j_v,k} - v^{n-1}_{y,\,i,j_v,k}}{h^2} \tag{112}$$

Handling a stencil like in Figure 21 is straightforward: the no-slip boundary condition implies

$$\left.\frac{\partial^2 u_x}{\partial x^2}\right|_{i_v,j,k}^{n} \approx \frac{v^n_{x,\,i_v+1,j,k} - v^{n+1}_{x,\,i_v,j,k} - v^{n-1}_{x,\,i_v,j,k}}{h^2} \tag{113}$$

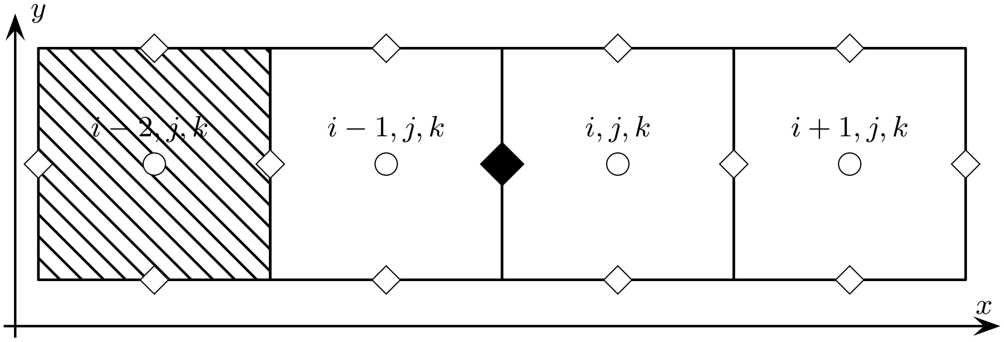

FIGURE 21. A stencil encountering a pore wall. The black filled diamond is the stencil's center.

4.5. **Discretization of boundary conditions at the sample boundary.**

4.5.1. *Dirichlet boundary condition.* With the staggered discretization grid described above, it is natural to approximate Dirichlet boundary condition,

$$\mathbf{v}|_{boundary} = \mathbf{v}_0 \tag{114}$$

at planes passing through the centers of the boundary voxels. For example at voxel N_x-3, N_y-1, k, Figure 22, one obtains

$$v_{x,\,N_x-3,N_y-1,k} = v_{0,x}, \quad v_{z,\,N_x-3,N_y-1,k} = v_{0,z} \tag{115}$$

and, in direction y,

$$\frac{v_{y,\,N_x-3,N_y-1,k} + v_{y,\,N_x-3,N_y,k}}{2} = v_{0,y} \tag{116}$$

The latter equation implies that, there is a single layer of ghost voxels on the downstream boundary in each direction. The last equation defines the respective value of the velocity:

$$v_{y,\,N_x-3,N_y,k} = 2v_{0,y} - v_{y,\,N_x-3,N_y-1,k} \tag{117}$$

4.5.2. *Robin boundary condition.* We model flow in a porous sample by immersing it in a stream of fluid flowing with velocity $\mathbf{v}_0$. Therefore, our boundary conditions should be formulated at infinity: $\mathbf{v}_\infty = \mathbf{v}_0$. However, the numerical domain is always finite. Therefore, we approximate the constant-velocity condition at infinity with a Robin-type condition

$$\mathbf{v} + \beta\frac{\partial \mathbf{v}}{\partial n} = \mathbf{v}_0 \tag{118}$$

Clearly, at a remote boundary, the normal derivative vanishes and one recovers the constant-velocity condition. We discretize the boundary condition, Equation (118), at the boundary voxel centers, which are marked with filled circles in Figure 22.

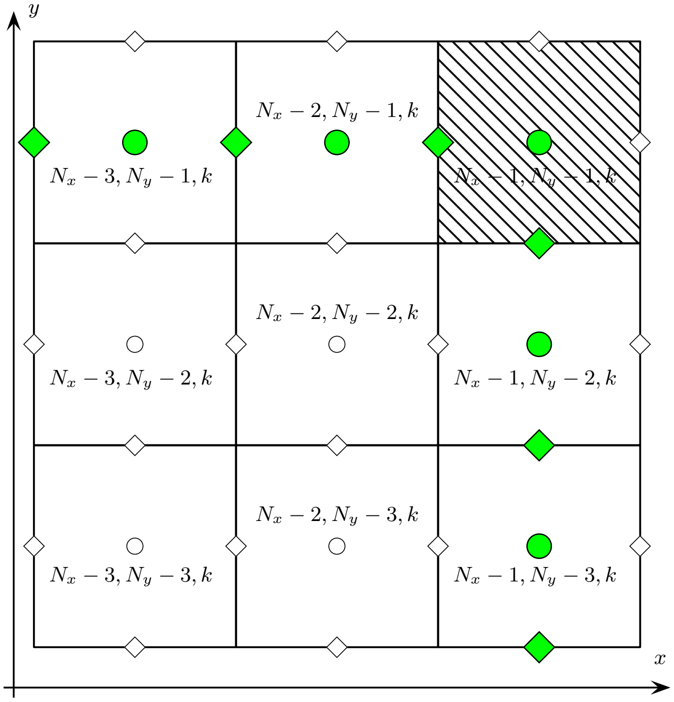

FIGURE 22. Discretization of the boundary: filled circles denote boundary nodes. The indices label the centers of voxels. The shaded corner voxel does not enter boundary condition approximation.

Approximation of boundary condition in the boundary voxel centers is rather straightforward. Fort example, for v_x at voxel N_x-1, N_y-2, k, one has

$$\left. v_x + \beta\frac{\partial v_x}{\partial n}\right|_{N_x-1,N_y-2,k} = \frac{v_{x,\,i_v-1,N_y-2,k} + v_{x,\,i_v,N_y-2,k}}{2} + \beta\frac{v_{x,\,i_v,N_y-2,k} - v_{x,\,i_v-1,N_y-2,k}}{h} + O(h^2) \tag{119}$$

where $i_v = N_x$. At a voxel boundary, the second-order approximation requires 3 nodes. For example,

$$\left. v_x + \beta\frac{\partial v_x}{\partial n}\right|_{N_x-1,j_v,k} = v_{x,\,N_x-1,j_v,k}$$

$$+\,\beta\frac{v_{x,\,N_x-1,j_v,k}-4v_{x,\,N_x-2,j_v,k}\text{‘}+3v_{x,\,N_x-3,j_v,k}}{2h}+O(h^2) \quad (120)$$

where $j_v = N_y - 1$. Both type of approximations do not involve time derivatives and are applied on the same layer n. Thus, from Equation (119)

$$v^n_{x,\,i_v,N_y-2,k} = \frac{2h}{2\beta+h}v_{x,\infty} + \frac{2\beta-h}{2\beta+h}v^n_{x,\,i_v-1,N_y-2,k} \quad (121)$$

and, from Equation (120),

$$v^n_{x,\,N_x-1,j_v,k} = \frac{2h}{3\beta+2h}v_{x,\infty} + \frac{4\beta}{3\beta+2h}v^n_{x,\,N_x-2,j_v,k} - \frac{3\beta}{3\beta+2h}v^n_{x,\,N_x-3,j_v,k} \quad (122)$$

These expressions must be used to replace respective boundary values in the discretization of differential equations.

Note that the staggering grid described above does not require evaluation of the velocities on the external boundaries of the vertex and edge boundary voxels. The reason is that the discretized second order derivatives of the velocities are evaluated only in the interior voxel boundaries. By the same reason, evaluation of the artificial density ρ at the corner nodes also can be skipped. Although these observation do not significantly reduce the amount of calculations, they do simplify the overall scheme, since discretization of the boundary conditions at the vertex voxels of the grid is the most cumbersome part.

4.6. **Scaling the velocity field.** Regardless of what numerical method is utilized, it is convenient to perform the computations for normalized dimensionless input data. In order to evaluate the results in physical units, they need an appropriate scaling. This section studies the physical scaling formulas.

Let us consider the Stokes equations, Equation (9). Let

$$\mathbf{v} = v_0\mathbf{V}, \quad x = DX,\ y = DY,\ z = DZ, \ \text{ and } p = p_0P \quad (123)$$

Then, in these new variables, Equation (9) has the following form:

$$\nabla P = \eta_0\nabla^2\mathbf{V} \quad (124)$$

where the viscosity coefficient in the new units, η_0, is

$$\eta_0 = \frac{\eta v_0}{p_0 D} \quad (125)$$

Note that this scaling does not affect the incompressibility condition, Equation (2).

We will assume that the discretized solution is in the new units. A pressure drop by one unit over one voxel size in the simulations gradient in the discretized equations corresponds to the pressure drop of the magnitude of $\frac{p_0}{D}$. Here D is the size of one voxel. In the simulations, the quantity η_0 is an adjustable computational parameter. Hence the converting factor for velocity is:

$$v_0 = \frac{p_0\eta_0}{\eta}D = \frac{p_0\eta_0}{D\eta}D^2 \quad (126)$$

To evaluate the Darcy velocity, the sum of fluxes over the pore voxels must be divided by the total area of the sample face. Darcy's law written down for the three pressure gradients in Equation (99) yields the following expression for the permeability tensor:

$$\underline{\underline{K}} = \eta\,\underline{\underline{\nabla p}}^{-1}\,\underline{\underline{W}} \quad (127)$$

where $\underline{\underline{\nabla p}}$ and $\underline{\underline{W}}$ are tensors constructed from the three pressure gradients and the respective three computed Darcy velocities. A substitution of the expression for η that follows from Equation (125) and taking into account Equations (99) and (126) yield

$$\underline{\underline{K}} = \frac{\eta_0 p_0 D}{v_0} \frac{D}{p_0} v_0 = D^2 \eta_0 \underline{\underline{W_0}} \tag{128}$$

where $\underline{\underline{W_0}}$ is the Darcy velocity evaluated in the units of the discretized system.

If, for example, one wants to simulate flow corresponding to 1% hydrostatic gradient, that is by $1000 \times 9.8 \times 10^{-2}$ Pa/meter, by running simulations with the pressure drop by one unit per voxel of size $D = 5$ μm, then for p_0 one has to put:

$$p_0 = 5 \times 10^{-6}\text{m} \times 1000 \frac{\text{kg}}{\text{m}^3} \times 9.8 \frac{\text{m}}{\text{s}^2} \times 10^{-2}\text{m}/1\text{m} = 4.9 \times 10^{-6} \text{ Pa} \tag{129}$$

4.7. **Testing the artificial compressibility algorithm.** To test the algorithm and to debug the code, we have chosen the classical Stokes problem of laminar flow in an infinite domain around a sphere of radius R. The velocity at infinity is equal $\approxeq_\infty$. No-slip boundary conditions are imposed on the surface of the sphere. It is known, that creeping-flow approximation adequately describes the flow near the sphere at sufficiently small distances from the surface of the sphere [39]. The creeping-flow solution is given by equation

$$\mathbf{u}(\mathbf{r}) = \mathbf{u}_\infty - \frac{3R}{4r} \left(\mathbf{u}_\infty + \mathbf{n}(\mathbf{u}_\infty \cdot \mathbf{n}) \right) - \frac{R^3}{4r^3} \left(\mathbf{u}_\infty - 3\mathbf{n}(\mathbf{u}_\infty \cdot \mathbf{n}) \right) \tag{130}$$

Here $\mathbf{r}$ is the radius-vector from the center of the sphere, and r is the distance from the center: $r = \|\mathbf{r}\|$. For the pressure, one has

$$p(\mathbf{r}) = p_\infty - \frac{3R}{2r^2} \eta \, \mathbf{u}_\infty \cdot \mathbf{n} \tag{131}$$

where p_∞ is the fluid pressure at infinity. If a reference system associated with the fluid, then the problem will have a more physically sound formulations.

To verify the algorithm, we simulate flow near a sphere of the radius of 5 voxel units. We put the sphere in the center of a $25 \times 25 \times 25$ voxel grid. At the outer boundaries, we impose Dirichlet conditions for velocities, which are merely the trace of the exact solution (130). On the sphere we assign zero-velocity condition. The stopping criterion requires that relative increments of l_2 norms are smaller than a prescribed tolerance value, ε_{tol}.

The plot on Figure 23 shows three profiles of the x component of the velocity versus y for three different va,lues of x. The bottom profile crosses the sphere, the top one is near the boundary, and the one in the middle corresponds to a midpoint between the sphere surface and the boundary. Note that neither the exact solution, nor the numerical one attain zero. The reason is that both solutions are evaluated on the same grid and none of the voxel centers occurs exactly on the surface of the sphere. The velocities obtained numerically are associated with the centers of the voxels by taking arithmetic mean values from the opposite boundaries of each voxel. Figure 24 shows similar comparison for the pressure profiles. The pressures have been plotted versus coordinate x aligned with the direction of the flow, for three different pairs of y and z. A cross-section of the vector field evaluated numerically is shown in Figure 25. Visually, a similar plot for exact solution is undistinguishable.

Even though the resemblance between the discretized sphere and an ideal spherical body can be questionable (see Figure 26 on the left), the comparison between numerical and exact solutions is encouraging. One has to note though that this accuracy has been achieved by applying rather stringent stopping criterion: $\varepsilon_{tol} = 7.5 \times 10^{-9}$. Relaxation of this criterion strongly affects the accuracy, Figure 27.

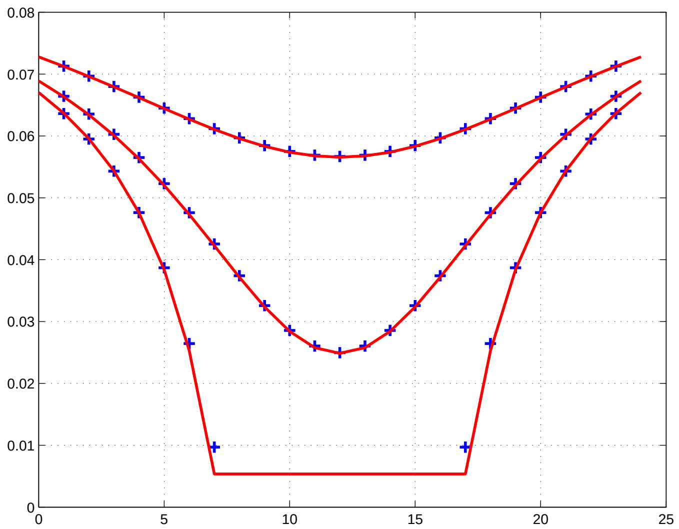

FIGURE 23. Tree velocity profiles: a comparison between exact solution (Eq. (130)), shown as a solid line, and numerical solution, pluses, in dimensionless units.

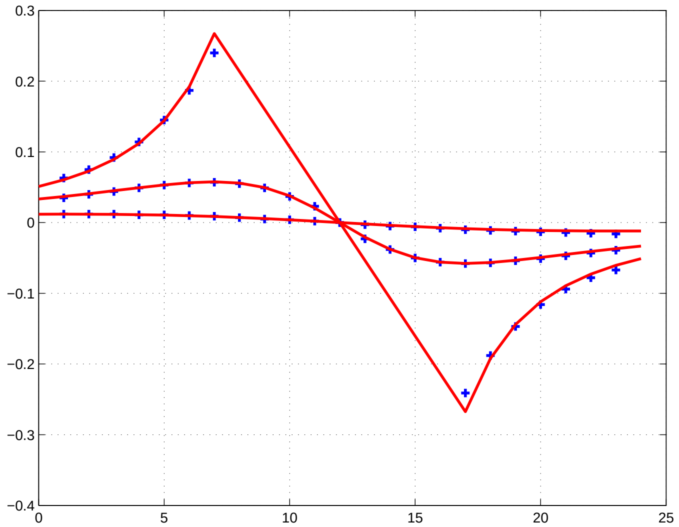

FIGURE 24. Tree pressure profiles: a comparison between exact solution (Eq. (130)), shown as a solid line, and numerical solution, pluses, in dimensionless units.

A refinement of the grid apparently requires more severe stopping criterion. Figure 28 shows the same velocity profiles evaluated numerically and through exact solution. Partitioning voxels by doubling the number of voxels in each direction results in an eight times larger grid. The numerical velocity profiles computed on the refined grid are not as accurate as those computed on the coarser one.

Further reduction of the stopping criterion by one order, $\varepsilon_{tol} = 7.5 \times 10^{-10}$ showed stabilization of the process with no improvement. Figure 29 shows that the Darcy velocity estimate in the downstream direction stabilizes. Darcy velocity in this case is an average value of the fluid velocity over the grid. The relative increments also stabilize near a value between 10^{-9} and 10^{-8}, Figure 30. A more detailed analysis of convergence reveals that the convergence in pressures is slower than that in velocities. This may be a consequence of the fact that the only time or space derivatives of the densities enter the artificial compressibility equations. Fixing the value of the pressure in some voxel is not a good solution since it imposes a constraint on the velocities through Equation (109).

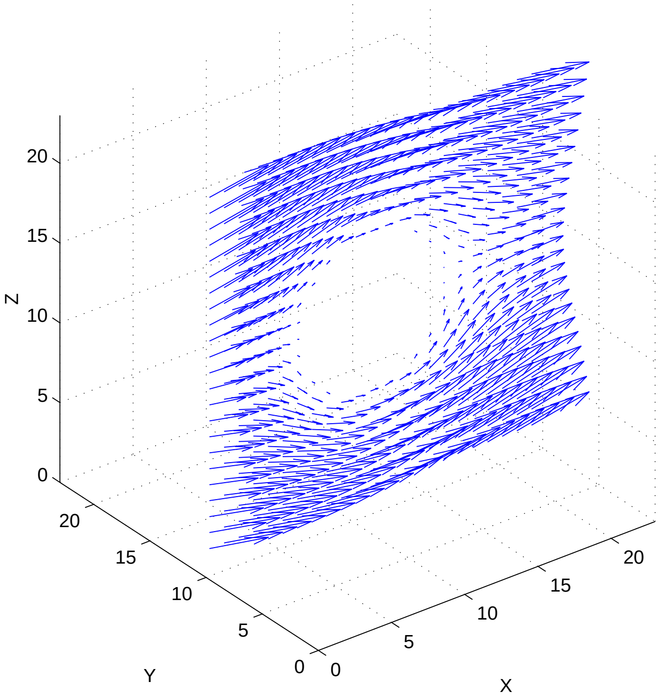

Figure 25. A central cross-section of the velocity field evaluated numerically.

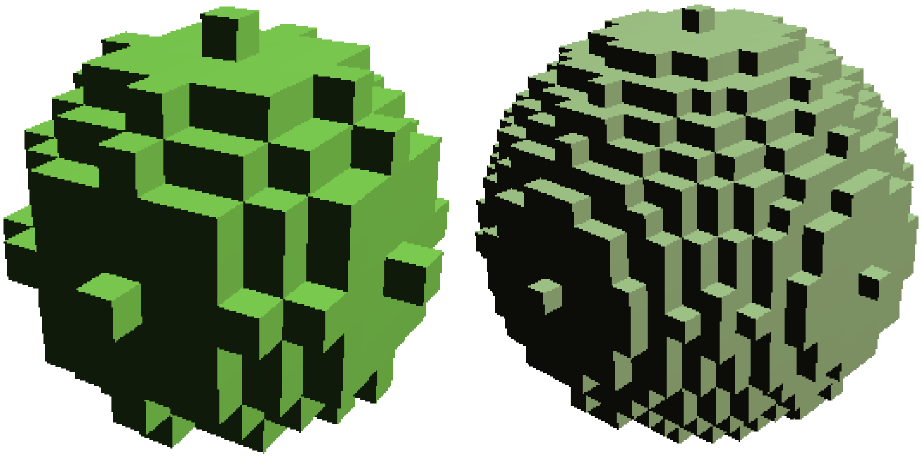

Figure 26. Discretized spheres of the radius of 5 voxel (on the left) and 10 (on the right) voxel units.

To summarize, one arrives at the following two principal conclusions. First, a reasonable accuracy of the numerical computations requires very stringent stopping criterion. Second, a stopping criterion producing a reasonable accuracy on a coarse grid may need an enhancement on a refined grid, since the latter has significantly more nodes. This makes achieving a reasonable accuracy of a numerical solution of Stokes equations on a large digital image especially challenging. The complexity of the pore space geometry only aggravates this difficulty.

The explicit nature of the numerical scheme makes the method of artificial compressibility suitable for parallel computations. However, the necessity for a stringent convergence criterion can make the implementation computationally expensive. We found that the performance of the projection method described in Section 3 is more robust, especially with appropriate selection of the

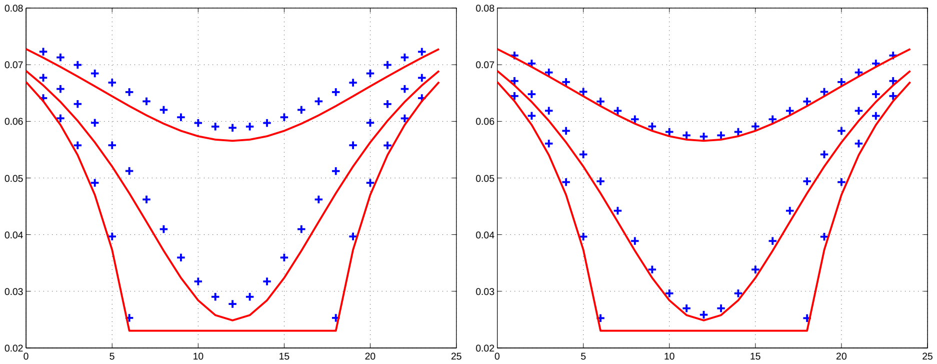

Figure 27. Velocity profiles shown in Figure 23 for relaxed stopping criterion: $\varepsilon_{tol} = 7.5 \times 10^{-7}$ on the left, and $\varepsilon_{tol} = 7.5 \times 10^{-7}$ on the right.

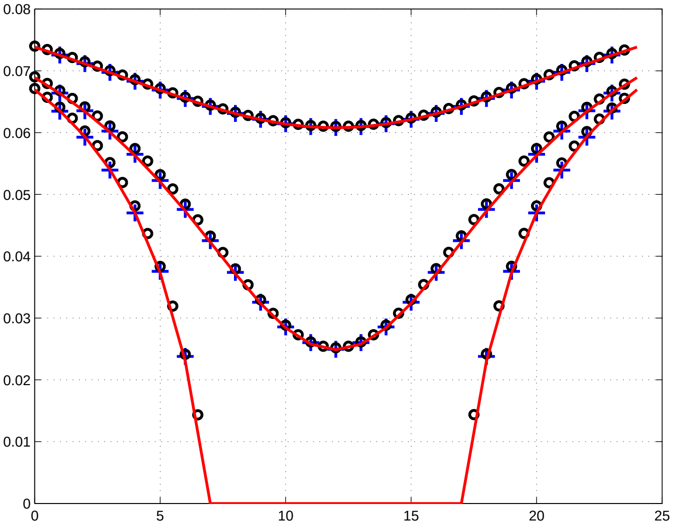

Figure 28. Velocity profiles evaluated numerically on coarse (pluses) and fine (circles) grids of voxels along with exact solution (solid line).

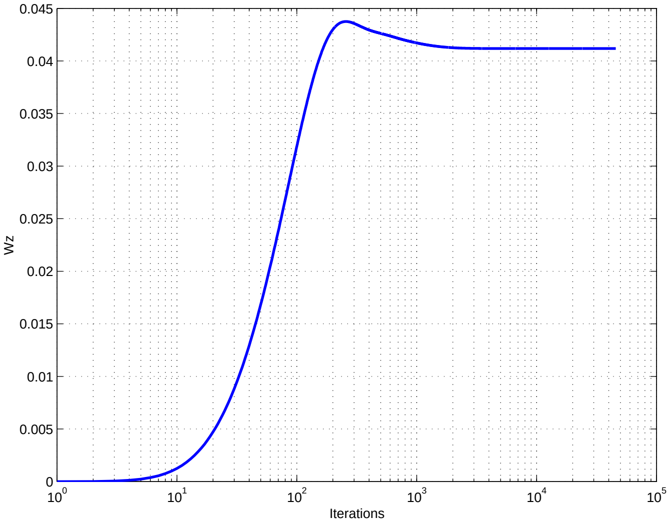

Figure 29. Stabilization of Darcy velocity estimate.

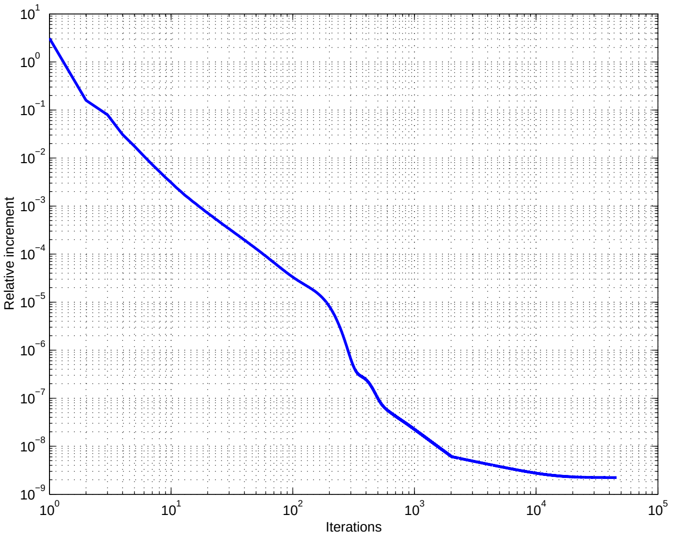

Figure 30. Stabilization of relative improvement near 10^{-9}.

preconditioner for the linear solver. At the same time, solving flow equations on a large data set can become computationally expensive. Development of efficient routines for solving flow equations would be a strong boost for the digital rock technology.

4.8. **Evaluation of permeability tensor.** To evaluate the permeability tensor, we run simulations with three different boundary conditions: with the velocity at infinity directed along each coordinate axis: x, y, and z. The obtained three Darcy velocities and respective pressure gradients yield the permeability tensor.

4.8.1. *Elimination of the dead ends.* The complexity of the computational domain may result in presence of pores or pore clusters which are only poorly connected to the inlet and outlet and have little impact on estimation of the permeability. If a connected pore cluster is connected to the rest of the pore space only through a single-voxel channel, the contribution of such cluster to the total volumetric flux is zero. Elimination of such dead-end clusters reduces the size of the computational domain but does not affect the estimation of Darcy velocity. Figure 31 shows two examples of such dead-end clusters in two dimensions. The solid voxels are dashed and the pores are blanc, whereas the bold solid line marks the pore-solid boundary. In Exhibit A, voxel a is connected to rest of the pores only through two faces: on the left and on the right. The pore voxels to the right from voxel a are mutually connected, and voxel a provides the only channel connecting this cluster to the rest of the pore space. In discretized steady flow, the velocities on all faces of voxel a are zero. Indeed, the right-hand face velocity must be zero since otherwise the fluid would accumulate in the cluster. One the left-hand side face, the velocity also must be zero since otherwise there would be fluid accumulation in voxel a. The zero velocity at the right-hand face of voxel a implies zero velocity in the entire cluster. Thus, the system of equations can be reduced by elimination of voxel a and the cluster from the computational domain and imposing a zero normal velocity condition at the left-hand face of voxel a. Voxel a in exhibit B also can be eliminated in a similar manner with no consequences for the flow and permeability.

The argument above suggests an algorithm of dead-end clusters search. First, all voxels with one or two connections to pores through nonadjacent faces should be found by scanning the entire domain. For each voxel with two connection, like in Figure 31 A, one should build two connected clusters starting on each side. A breadth-first type algorithm similar to one described in [61] can be applied. If either of these clusters is disconnected from the inlet and outlet, it is a dead end and

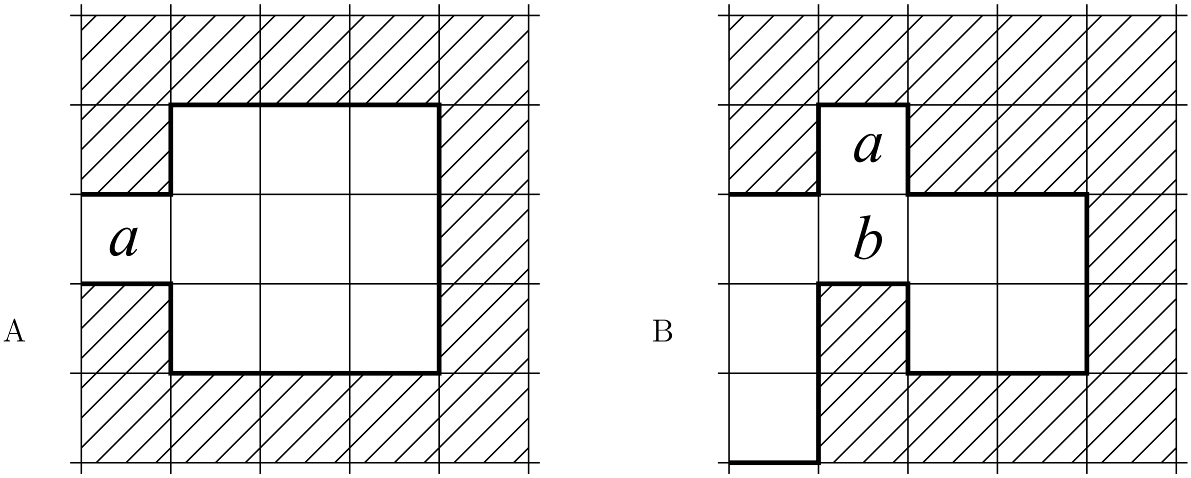

Figure 31. Examples of dead-end voxel configurations.

can be removed from the computational domain. It is also a dead end if either both clusters are connected only to the inlet, or both clusters are connected only to the outlet. This connectivity analysis must be applied iteratively, until no more dead-end voxels or clusters are found. For example, voxel b in Figure 31 B has three open boundaries. However, one of these boundaries becomes closed once voxel a is removed. Although neither voxel b nor the entire pore cluster to the right is removed by the first scan, both are defined as dead ends and removed during the second scan.

4.8.2. *Boundary conditions, Darcy velocity, and evaluation of permeability.* Pore-scale flow simulations produce an estimate of the permeability tensor. Pressure gradient can be applied by assigning Dirichlet boundary conditions at the inlet and outlet boundaries of the domain. The other boundaries can be sealed by "wrapping" the computational domain with a layer of solid voxels. The averaging of the computer velocity field provides an estimate of Darcy velocity. The vector of average velocity is not necessarily aligned with the pressure gradient. Running flow simulations for three orthogonal pressure gradients yields an estimate of permeability tensor. On a large domain, this procedure can be applied to subsamples and an effective permeability tensor can be obtained by the averaging procedure described in Section 6 below.

Instead of Dirichlet boundary conditions for pressures, one can simulate flow at a givel flow rate. Indeed, since the Stokes equations are linear, one can run dimensionless simulations for a some inlet–outlet pressure drop, and linearly scale the magnitude of this pressure drop to match the desired flow rate. In this study, the lateral boundary conditions in simulations modeled isolation of the sample by a sleeve. Alternatively, one can impose periodic boundary conditions. It means that the modeling domain indefinitely increased by repeating the sample geometry periodically. Since the opposite faces of the sample do not need to have the same geometry, the sample can be mirror-reflected at each boundary. Thus, to mimic periodic boundary conditions at the lateral boundaries, by virtue of the symmetry of mirror reflection, it suffices to impose zero normal component condition for velocities.

4.9. **Implementation.** The numerical methods described in the previous sections are implemented in computer codes. The procedure goes in the following way.

(1) The user provides an instruction text file with information about the input data and values for tunable parameters.
(2) First, the program runs a search for dead-end clusters and voxels as described in Section 4.8.1.

(3) Second, flow simulations run on the "cleaned up" domain for three orthogonal pressure gradients.
(4) A estimate of the permeability tensor is assembled based on three Darcy velocity vectors obtained by averaging respective local velocity fields.
(5) The absolute permeability is estimated by averaging the diagonal elements of the tensor.
(6) Optionally, the output can also include the velocity field and pressure distribution for visualization with ParaView [29] ot similar software. The velocity field is exported in VTK format [55], whereas the pressures are saved in a raw floating-point binary file.

The tunable parameters the user has to provide include the convergence criterion and maximum number of iterations the linear solver. These parameters are used for solving discretized Poisson equation (59) and Laplace equation (137). To increase the efficiency of the method of projections, the convergence requirements for Poisson equation (59) are relaxed on early iterations described in equations (56)–(59). The program can analyze the entire data set or its fragment depending on the instructions in the user-provided text file.

The program is called with a parameter which defines which of the following tasks has to be performed:

Task 1: Estimate the absolute permeability tensor.
Task 2: Estimate the relative permeability curves.
Task 3: Estimate the permeability of subsamples.
Task 4: Estimate an effective absolute permeability by solving Equation (137) on a grid with permeability tensor denied in each grid cell.
Task 5: Estimate absolute permeability with slip for different values of the slippage coefficient.

The instructions file is different for each task. Task 2 needs results of MIS calculations as input data. The MIS calculations produce a number of files describing the fluid distribution at different capillary pressures, and the code evaluates the permeability of the portion of the pore space occupied by each fluid. The input data for Task 4 can be either generated by running Task 3 or provided independently.

5. Modeling two-phase capillary equilibrium with the method of Maximal inscribed spheres

In capillary equilibrium, the mean curvature interface between two immiscible fluids is determined by the capillary pressure through Yang–Laplace equation [17, 39]. This law establishes a one-to-one correspondence between the radius of the fluid-fluid interface curvature and the magnitude of capillary pressure. Te method of maximal inscribed spheres (MIS) employs this correspondence to model capillary-equilibrium two-phase fluid distribution.

5.1. Fully wet conditions: zero contact angle.

For zero contact angle, the idea of implementation of MIS is simple. For a given capillary pressure p_c, one seeks the part of the pore space that can be covered by spheres of the radii equal to or greater than the radius determined by p_c through the Young–Laplace equation. The portion of the pore space determined this way is occupied by the nonwetting fluid. The complementary part of the pore space is, respectively, occupied by the wetting fluid, and its relative volume determines the value of saturation. The plot of saturations versus p_c, obtained in this manner, defines a computed capillary pressure curve. Figure 32 schematically illustrates the idea.

Note that the key operation in this procedure is the determination of relative volume. Its implementation into an algorithm and computer code can be done independent of capillary pressure, in dimensionless units. The respective capillary pressure is dimensionless, but can be converted into physical units using the image resolution (voxel size) and the coefficient of surface tension. MIS calculations can model different fluid displacement scenarios an a quasi-static manner where the

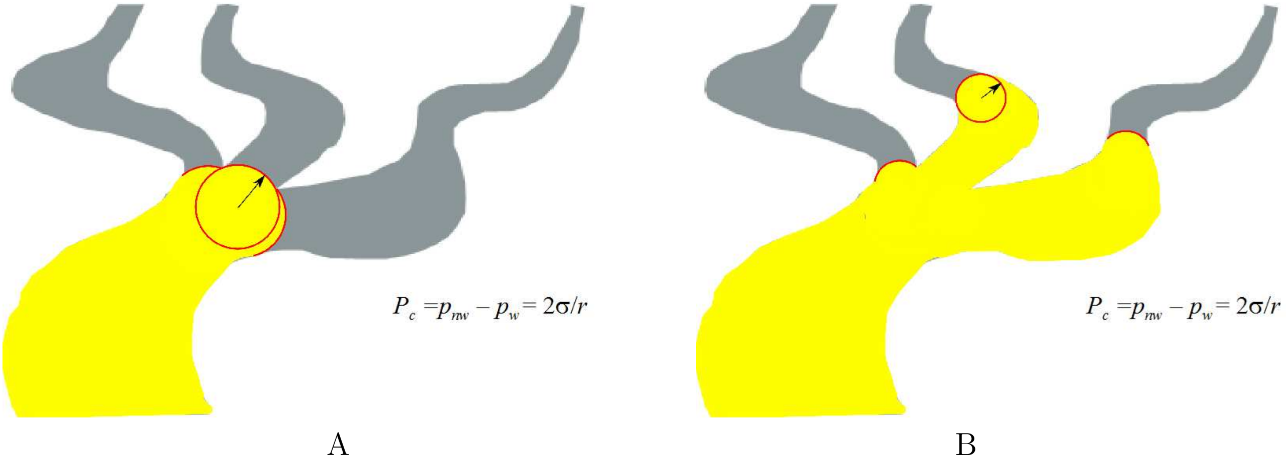

Figure 32. A schematic 2D illustration of the method of maximal inscribed spheres: The area swept by inscribed spheres of a give radius determines the part of the pore spcae occupied by the nonwetting fluid. The radius decreases at increasing capillary pressure. The picture in Exhibit A corresponds to a capillary pressure lower than that in exhibit B.

process is presented as a sequence of equilibrium configurations. For example, drainage displacement can be modeled by accounting only for the nonwetting phase saturation connected to the boundaries. Drainage displacement can be modeled with an invasion percolation algorithm involving cluster search methods [59]. Ordinary percolation is more suitable for modeling a two-phase fluid distribution resulting from either from gas exsolution or liquid dropout, where the presence of fluid phases is the consequence of local thermodynamic equilibrium rather than fluid displacement by flow.

To handle binary digital data, the spheres are discretized, see Figure 26. The shape of a small radius sphere discretization only remotely resembles an ideal round sphere. Fluid distribution at high capillary pressure is likely to be affected by microporosity, which is frequently beyond the resolution of imaging tools. Thus, the capillary pressure predictions for low wetting fluid saturation are less reliable than for medium and high saturations. In addition, the MIS-calculated fluid-fluid interface can be only considered as an first-order approximation to the complex geometry of real interfaces. Nevertheless, analysis of the pore geometry of a FIB/SEM scanned sample of chalk produced results, which are in good agreement with experimental data [70]. Moreover, MIS-calculated fluid distribution can mimic fluid distribution obtained by micro CT imaging [65]. Figure 33 A shows fluid distribution in a CO_2 flooding experiment imaged by Jonathan Ajo-Franklin at the Advanced Light Source facility of LBNL. Figure 33 B shows fluid distribution predicted by MIS calculations. The MIS calculations simulated drainage displacement with the direction of flow aligned with the core orientation in the experiment. Although there is no rigorous one-to-one correspondence between the experimental and computed fluid distributions, there is strong similarities between exhibits A and B of Figure 33.

5.2. **Accounting for mixed wettability.** Wettability is the property of solid materials to contact preferentially, one fluid relative to the other. Wettability is usually characterized by a contact angle formed by fluid-fluid interface relative to the solid boundary. Contact angle is determined by the material properties of the fluids and solid if observed on an ideally smooth surface in contact with a sufficiently large droplet of the nonwetting phase. An ideal smooth surface is almost impossible in most reservoir rocks. Thus, at a given temperature and pressure, the solid surface roughness also can have an impact on the effective contact angle [1, 2]. To model capillary equilibrium fluid

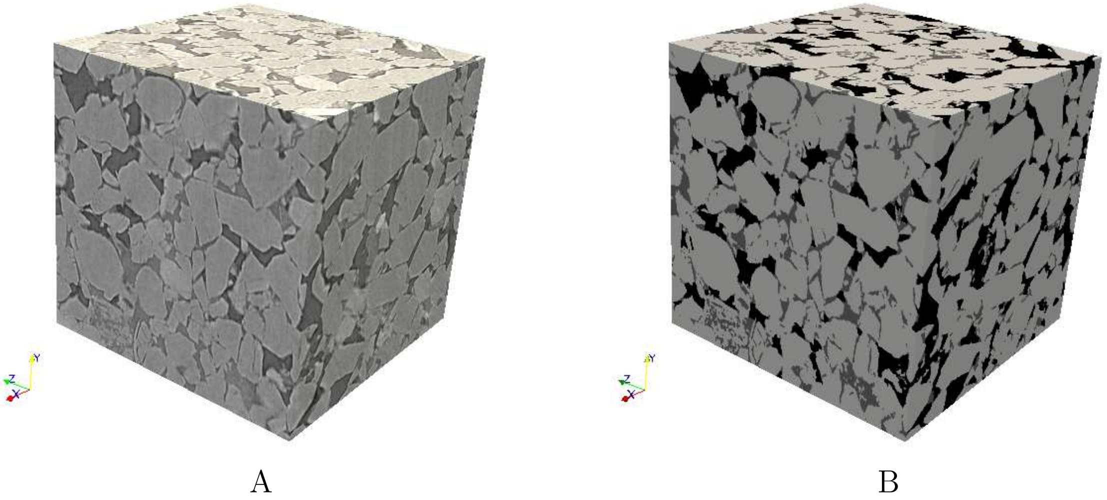

FIGURE 33. Gray-scale micro CT image (A) and MIS calculated two-phase fluid distribution in a $2 \times 2 \times 2$ mm^3 sample of sandstone. The 4.5 μm resolution CT data were acquired by Jonathan Ajo-Franklin at the Advanced Light Source facility of LBNL.

distribution for a non-zero contact angle, the MIS procedure needs a modification, which is described in this section.

Let us assume a contact angle θ, $0 \leq \theta < \pi/2$. Figure 34 illustrates the idea of the modified MIS method. First, for a given radius R, all inscribed spheres are determined in the same was as described above for a zero contact angle. Then, each inscribed sphere is expanded by a factor of $(\cos\theta)^{-1}$, and the nonwetting fluid saturation is evaluated based on these extended spheres. Each extended shpere it tested on connectivity: only the part of the volume that is connected to the original center is accounted for in evaluation of the saturation.

Both, the heterogeneous mineralogy, and the roughness of pore walls, practically prohibit a one-hundred percent proof rigorous evaluation of the contact angle in natural rocks. Thus, the proposed modification of MIS calculation is a compromise between complexity and computational feasibility. It is a reasonable first approximation only. Level sets method (see [34, 49]) are likely to more accurately describe the local fluid-fluid interfaces of constant mean curvature, but may be too demanding computationally for handling large data sets. MIS calculations can process gigabytes of data on a desktop-size personal computer.

In the literature, the impact of wettability on the capillary pressure curve is usually modeled by an additional factor of $\cos\theta$ in front of the Leverett's $\mathcal{J}$-function [41]. The plots in Figure 35 show dimensionless capillary pressures evaluated with the described procedure against dimensionless capillary pressures evaluated for a zero contact angle and multiplied by a factor of $\cos\theta$ for $\theta = 45°$. The straight lines correspond to ideal correlation 1. The plots show that the correlation is good for low capillary pressures, and deteriorates as the capillary pressure goes up. The deviation patterns are different for drainage (only connected nonwetting phase, Figure 35 A) and imbibition (both connected and dispersed nonwetting phase, Figure 35 B) capillary pressure curves.

5.3. **Evaluation of the relative permeability curves.** In two- or multi-phase flow in natural rocks or other porous materials, the flow is described by the generalized Darcy's law. The foundation of the theory of multi-phase flow in porous media have been developed by Muskat and Meres [45] and Leverett [40]. Consider, for example, simultaneous flow of water and oil. Since each fluid occupies only a part of the pore space, the permeability to this fluid is different from the absolute

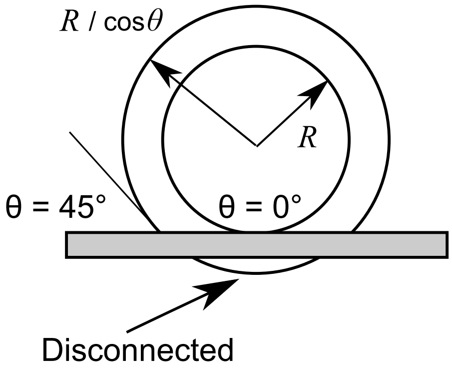

Figure 34. Modeling non-zero contact angle: connectivity needs to be checked after stretching an inscribed sphere by a factor of $\cos\theta^{-1}$. If detected, the disconnected part are removed from the evaluation of saturation.

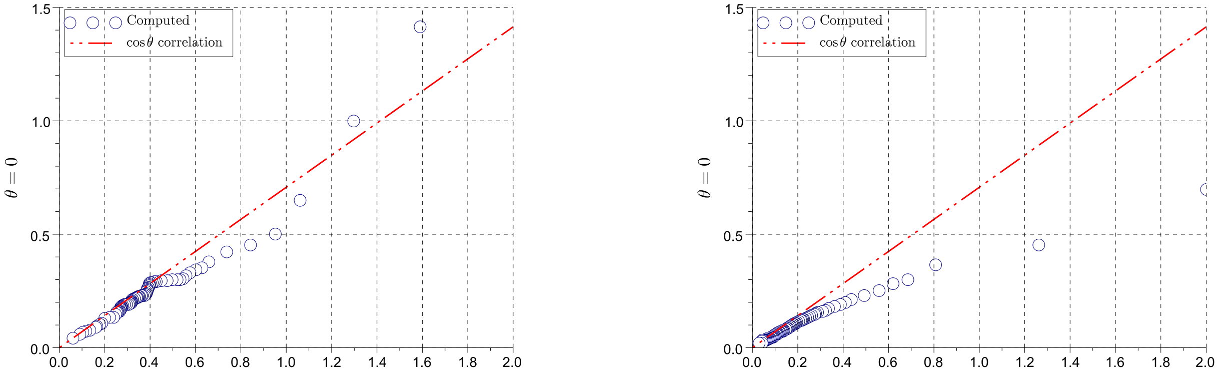

A B

Figure 35. Examples of $\cos\theta$ correlation and numerically evaluated capillary pressure. Both, for drainage (A) and imbibition (B) the correlation deviates from 1 at higher capillary pressures.

permeability of the rock. A dimensionless relative permeability is a correction factor, so that the Darcy's law for each fluid has the form:

$$u_o = -\frac{k_o k}{\mu}\nabla p_o, \qquad u_w = -\frac{k_w k}{\mu}\nabla p_w \tag{132}$$

The relative volume of the pore space occupied by each fluid is its saturation. According to the classical theory, both relative permeability factors, k_o and k_w, are functions of fluid saturation. Since the sum of both saturations is identically one, water saturations, S_w, completely characterizes the volumetric fluid distribution. Thus, one can write

$$k_o = k_o(S), \qquad k_w = k_w(S) \tag{133}$$

where $S = S_w$.

One of the main assumptions of the classical theory of multi-phase flow in porous media is local equilibrium of the fluid distribution. Saturation is only one of the parameters describing this equilibrium. The geometry of the fluid-fluid interfaces are characterized by the capillary pressure, the flow rate, and the history of fluid displacement [8, 48].

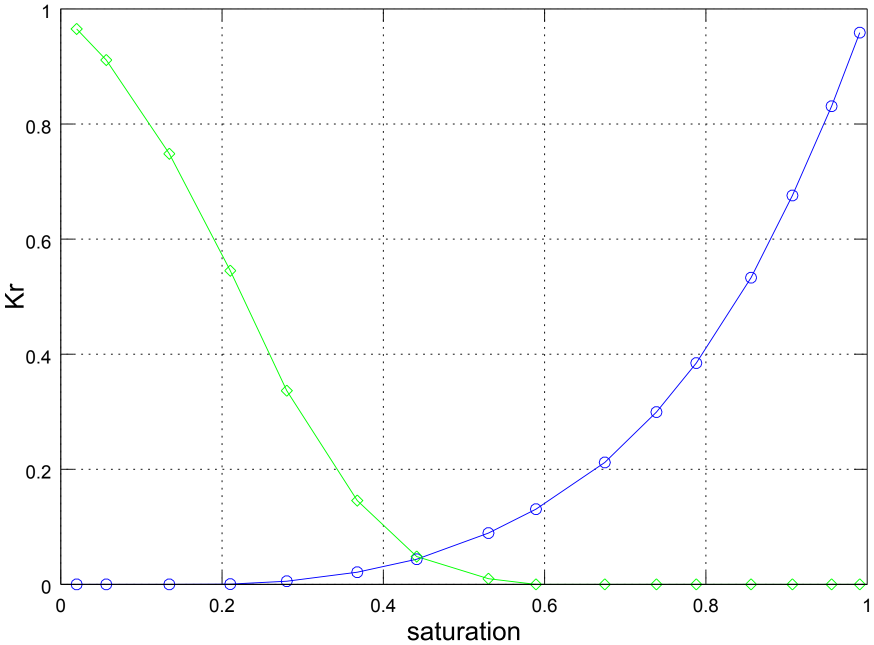

Figure 36. An example of computed relative permeability curves

In this work, we assume that local equilibrium is entirely defined by the capillary pressure. In such a case, the distribution of the fluids in the pore space can be estimated using the method of maximal inscribed spheres described above. MIS calculations produce a number of capillary-equilibrium fluid distributions. Each such distribution is defined by the lists of voxels occupied by the wetting and nonwetting fluid phases. At each saturation, all voxels occupied by one fluid can be considered as a stand-alone pore space. Thus, the permeability of this system of voxels scaled by the absolute permeability of the entire pore space is an approximation to the relative permeability factor.

The following procedure is proposed to evaluate the relative permeability curves numerically.

(1) Estimate the absolute permeability of the pore space;
(2) For a number of capillary pressures, calculate fluid distribution using MIS algorithm and evaluate the respective saturations;
(3) For each fluid distribution, evaluate the permeability to each fluid;
(4) Express the relative permeability as a function of saturation.

Figure 36 shows one example of calculations for a computer-generated sample. Figure 37 shows plots of numerical results for CT images of sandstone show and a number of experimental points obtained in coreflood laboratory experiments. The images of the rock pore space used in the computations have been acquired not from the same samples. So, the comparison can be only qualitative. One can see that the computed relative permeability curves, which are solid curves with various markers on the plots, are in the same range as the experimental points. The variability of the computed relative permeabilities is similar to that of the data. The partitioning of the 3D image into layers was done differently for different computed curves. The outlier pair of relative permeability curves marked with squares has been obtained from a smaller fragment of the image than the other curves.

6. Evaluation of the permeability tensor by subsampling

In this section, we assume that a large image is split into smaller fragments, and the permeability tensor already has been evaluated on each fragment. We describe a procedure of upscaling of these

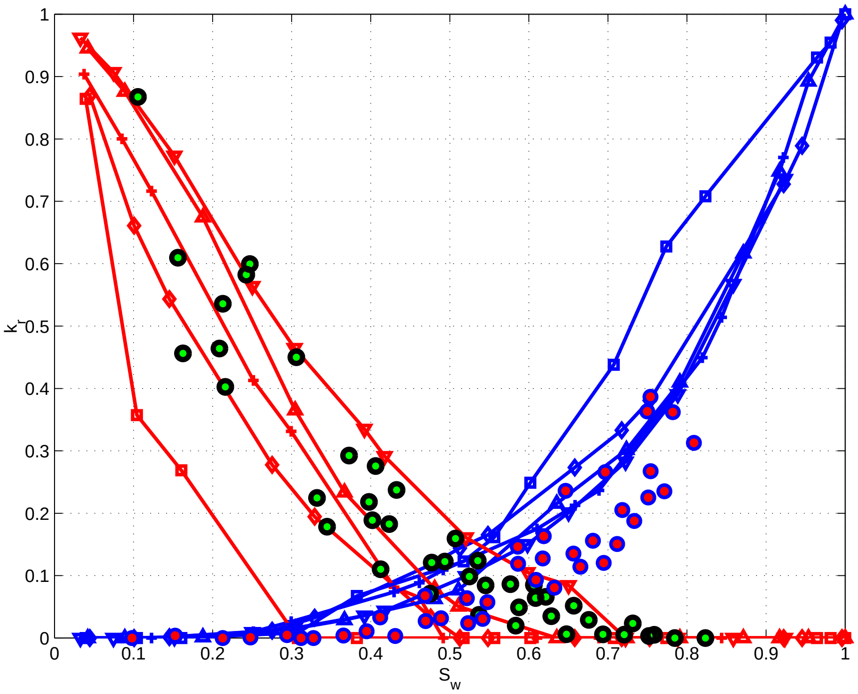

FIGURE 37. Computed relative permeability curves and laboratory data (circles).

partial results over the entire image. That is the permeability of the whole image is estimated using the permeability tensors of the fragments. The partition of the entire image into fragments should be done in such a way that the geometry of the pore space is simple enough. At the same time, each fragment has to be representative in order to make the computations sensible.

The usefulness of doing computations by parts can be illustrated by the following simple calculation. If the computational complexity, that is, the number of operations, is proportional to the size of the image raised to a power $\chi > 1$, then the total number of operations on all parts is

$$N_{\text{total}} = N_{\text{parts}} \left(\frac{N_{\text{image}}}{N_{\text{parts}}} \right)^{\chi} = N_{\text{image}}^{\chi} \frac{1}{N_{\text{parts}}^{\chi-1}} \tag{134}$$

The first factor on the right-hand side does not depend on the partition, whereas the second decreases as the partition is refined.

Our next objective is to obtain numerically a solution to a steady-state flow problem. According to Darcy's law, the Darcy velocity is a linear function of the pressure gradient:

$$u = -\frac{K}{\mu} \nabla p \tag{135}$$

Combining Equation (135) with incompressibility condition

$$\nabla \cdot u = 0 \tag{136}$$

we obtain a Laplace equation for the pressures

$$\nabla \left(\frac{K}{\mu} \nabla p \right) = 0 \tag{137}$$

where μ is the fluid viscosity. The Dirichlet boundary conditions are formulated in a way, similar to the one used above. For three pressure gradients, Equations (99), we impose $p = p_{\text{in}}$ and $p = p_{\text{out}}$ condition at the inlet and outlet faces, which are orthogonal to the pressure gradient, and linearly interpolate between p_{in} and p_{out} on all other boundaries.

The solution to this boundary-value problem for each ∇p yields a mean Darcy velocity, Eq. (135). Multiplication of this velocity by μ produces the respective column of the upscaled permeability tensor. The absolute permeability of the rock does not depend on the viscosity of fluid. Thus, to simplify the computations, one can put $\mu = 1$, regardless of the units used in computations.

Since a numerical scheme of solving Darcy flow equations should handle full permeability tensors associated with the grid cells, standard finite difference schemes do not apply straightforwardly. Here, we develop a procedure based on the support-operators method [25, 58]. In general, the discretization of the flux by support-operators method is a function of the entire grid. However, even for anisotropic permeability, the equations of support-operators method can be resolved explicitly on a rectangular grid. Consequently, in the case under consideration, the flux operator is local, that significantly simplifies the computations.

6.1. **Discretization of the Darcy's law.** The next step is to discretize the right-hand side of Equation (135) taking into account the fact that the tensor on the right-hand side is full. Again, we put $\mu = 1$ for the sake of simplicity.

First, consider a grid block, which is inside the domain. The objective is to find a discretized version of the normal component of the Darcy velocity defined by equation (135) evaluated in the centers of grid cell boundaries.

To make the scheme conservative, the flux operator discretization is linked to the discretization of the divergence by the Green–Gauss–Ostrogradskii theorem [68]. According to this theorem, for an arbitrary simply-connected domain Ω, the gradient of a scalar field p and the divergence of a vector field $\mathbf{v}$ satisfy the integral relationship

$$\int_\Omega \mathbf{v} \cdot \nabla p \, dV + \int_\Omega p \nabla \cdot \mathbf{v} \, dV = \int_{\partial\Omega} p\mathbf{v} \cdot d\mathbf{S} \tag{138}$$

Here dV and $d\mathbf{S}$ are volume and surface elements, where the latter is oriented by the outward unit normal.

First, we rewrite Equation (138) in an equivalent form:

$$\int_\Omega K^{-1}\mathbf{v} \cdot K\nabla p \, dV + \int_\Omega p \nabla \cdot \mathbf{v} \, dV = \int_{\partial\Omega} p\mathbf{v} \cdot d\mathbf{S} \tag{139}$$

The last equation is valid for any non-degenerate symmetric tensor K. For a non-symmetric tensor, the K^{-1} on the left-hand side must be replaced with the transpose tensor. The next step is to discretize the relationship in the last equation for the volume marked by bold lines in Figure 38. The second integral on the left-hand side vanishes just because the vector field is constant. To account for the heterogeneity of the permeability, the term $K^{-1}\mathbf{v}$ in the first integral on the left-hand side of Equation (139), which must be evaluated at the interface between the grid cells located is inside the volume shown in Figure 38, is approximated with

$$\left(K^{-1}\mathbf{v}\right)_{i+1/2,j,k} \approx \frac{1}{2}\left(K^{-1}_{i,j,k} + K^{-1}_{i+1,j,k}\right)\mathbf{v} \tag{140}$$

First, choose a constant velocity field

$$\mathbf{v}_x = (1, 0, 0)^T \tag{141}$$

which is aligned with the shift of the volume relative to the grid. To come up with a discretized version of the last equation, we replace the integrals with cubature and quadrature formulae. Note, that $\mathbf{v}_x \cdot d\mathbf{S}$ is non-zero only for two faces of the volume. The centers of these faces are in the centers of the grid cells with indices (i, j, k) and $(i + 1, j, k)$. Thus, the integral on the right-hand of Equation (139) can be approximated by

$$\int_{\partial\Omega} p\mathbf{v}_x \cdot d\mathbf{S} \approx (p_{i+1,j,k} - p_{i,j,k})h^2 \tag{142}$$

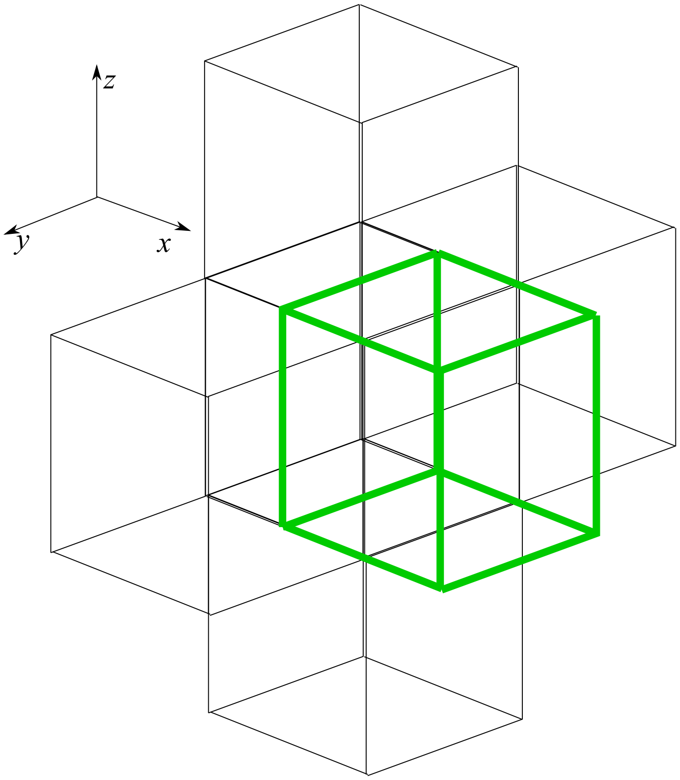

FIGURE 38. A shifted grid cell for approximation of the normal component of the Darcy velocity. The regular grid cells are shown as thin lines, whereas the grid cell shown with bold lines is centered in the center of one of the faces of the regular grid cells.

where h is the length of the edge of the cubic grid cells. Thus,

$$\frac{1}{2}\left(K^{-1}_{i,j,k}+K^{-1}_{i+1,j,k}\right)\mathbf{v_x}\cdot(K\nabla p)_{i+1/2,j,k}\approx\frac{1}{h}(p_{i+1,j,k}-p_{i,j,k}) \tag{143}$$

By applying an analog of the trapezoidal rule of numerical integration and approximation

$$p_{i,j+1/2,k}=\frac{p_{i,j,k}+p_{i,j+1,k}}{2}+O(h^2),\quad p_{i,j,k+1/2}=\frac{p_{i,j,k}+p_{i,j,k+1}}{2}+O(h^2) \tag{144}$$

one obtains two more approximations of the the integral on the right-hand of Equation (139):

$$\int_{\partial\Omega}p\mathbf{v}_y\cdot d\mathbf{S}\approx\left[\frac{1}{4}(p_{i+1,j+1,k}+p_{i,j+1,k})-\frac{1}{4}(p_{i+1,j-1,k}+p_{i,j-1,k})\right]h^2 \tag{145}$$

for $\mathbf{v}_y=(0,1,0)^T$, and

$$\int_{\partial\Omega}p\mathbf{v}_z\cdot d\mathbf{S}\approx\left[\frac{1}{4}(p_{i+1,j,k+1}+p_{i,j,k+1})-\frac{1}{4}(p_{i+1,j,k-1}+p_{i,j,k-1})\right]h^2 \tag{146}$$

for $\mathbf{v}_z=(0,0,1)^T$. Thus, Equation (143) is complemented by two more equations

$$\frac{1}{2}\left(K^{-1}_{i,j,k}+K^{-1}_{i+1,j,k}\right)\mathbf{v_y}\cdot(K\nabla p)_{i+1/2,j,k}\approx\frac{1}{h}\left(\frac{p_{i+1,j+1,k}+p_{i,j+1,k}}{4}-\frac{p_{i+1,j-1,k}+p_{i,j-1,k}}{4}\right) \tag{147}$$

$$\frac{1}{4}\left(K^{-1}_{i,j,k}+K^{-1}_{i+1,j,k}\right)\mathbf{v_z}\cdot(K\nabla p)_{i+1/2,j,k}\approx\frac{1}{h}\left(\frac{p_{i+1,j,k+1}+p_{i,j,k+1}}{4}-\frac{p_{i+1,j,k-1}+p_{i,j,k-1}}{4}\right) \tag{148}$$

Since the vectors $\mathbf{v_x}$, $\mathbf{v_y}$, and $\mathbf{v_z}$, compose an identity tensor, one finally obtains

$$(K\nabla p)_{i+1/2,j,k} \approx \frac{1}{h}\left[\frac{1}{2}\left(K^{-1}_{i,j,k} + K^{-1}_{i+1,j,k}\right)\right]^{-1} \begin{pmatrix} p_{i+1,j,k} - p_{i,j,k} \\ \dfrac{p_{i+1,j+1,k} + p_{i,j+1,k}}{4} - \dfrac{p_{i+1,j-1,k} + p_{i,j-1,k}}{4} \\ \dfrac{p_{i+1,j,k+1} + p_{i,j,k+1}}{4} - \dfrac{p_{i+1,j,k-1} + p_{i,j,k-1}}{4} \end{pmatrix} \tag{149}$$

Finally, only the normal component of the Darcy velocity enters the mass balance equation, so

$$(K\nabla p)^x_{i+1/2,j,k} \approx \frac{1}{h}\left\{\left[\frac{1}{2}\left(K^{-1}_{i,j,k} + K^{-1}_{i+1,j,k}\right)\right]^{-1}\right\}^x \cdot \begin{pmatrix} p_{i+1,j,k} - p_{i,j,k} \\ \dfrac{p_{i+1,j+1,k} + p_{i,j+1,k}}{4} - \dfrac{p_{i+1,j-1,k} + p_{i,j-1,k}}{4} \\ \dfrac{p_{i+1,j,k+1} + p_{i,j,k+1}}{4} - \dfrac{p_{i+1,j,k-1} + p_{i,j,k-1}}{4} \end{pmatrix} \tag{150}$$

Where the superscript ^{x} denotes the first column of the matrix. On the right-hand side, it merely reduces to the top row of the tensor in the square brackets. Similar expressions can be obtained for the other two components of the flux operator:

$$(K\nabla p)^y_{i,j+1/2,k} \approx \frac{1}{h}\left\{\left[\frac{1}{2}\left(K^{-1}_{i,j,k} + K^{-1}_{i,j+1,k}\right)\right]^{-1}\right\}^y \cdot \begin{pmatrix} \dfrac{p_{i+1,j+1,k} + p_{i+1,j+1,k}}{4} - \dfrac{p_{i-1,j,k} + p_{i-1,j,k}}{4} \\ p_{i,j,k} - p_{i,j+1,k} \\ \dfrac{p_{i,j+1,k+1} + p_{i,j,k+1}}{4} - \dfrac{p_{i,j+1,k-1} + p_{i,j,k-1}}{4} \end{pmatrix} \tag{151}$$

$$(K\nabla p)^z_{i,j,k+1/2} \approx \frac{1}{h}\left\{\left[\frac{1}{2}\left(K^{-1}_{i,j,k} + K^{-1}_{i,j,k+1}\right)\right]^{-1}\right\}^z \cdot \begin{pmatrix} \dfrac{p_{i+1,j,k+1} + p_{i+1,j,k}}{4} - \dfrac{p_{i-1,j,k+1} + p_{i-1,j,k}}{4} \\ \dfrac{p_{i,j+1,k+1} + p_{i,j+1,k}}{4} - \dfrac{p_{i,j-1,k+1} + p_{i,j-1,k}}{4} \\ p_{i,j,k+1} - p_{i,j,k} \end{pmatrix} \tag{152}$$

The superscripts ^{y} and ^{z} denote the second and third columns of the tensor.

If the permeability tensors $K_{i,j,k}$ and $K_{i+1,j,k}$ are just scalar factors, then Equation (150) reduces to the harmonic mean approximation conventionally used by numerical modelers [53]. Indeed, a scalar tensor is the product of a scalar factor and an identity tensor. Thus, the second and the third elements of the top row of the permeability tensor on the right-hand side of Equation (150) are equal to zero. Thus, one obtains

$$(K\nabla p)^x_{i+1/2,j,k} \approx \left[\frac{1}{2}\left(\frac{1}{K_{\,i,j,k}} + \frac{1}{K_{\,i+1,j,k}}\right)\right]^{-1} \frac{p_{i+1,j,k} - p_{i,j,k}}{h} \tag{153}$$

6.2. **Discretization of Laplace operator.** Laplace operator $\nabla^2 p = \nabla \cdot (K\nabla p)$ is a superposition of the divergence and Darcy flux. A discretization of the latter has been described in the previous section. The divergence of a vector field v can be approximated in the following way:

$$\nabla \cdot v \sim \frac{1}{|V_{ijk}|}\int_{\partial V_{ijk}} v \cdot n\, d\sigma \tag{154}$$

Here $|V_{ijk}| = d^3$ is the volume of the cell V_{ijk} centered at (i, j, k), and $n\, d\sigma$ is its surface element with unit outer normal n. To numerically evaluate the integral on the right-hand side of Equation (154), one can apply a cubature formula with equal weights. Thus,

$$\nabla \cdot \mathbf{v} \approx \frac{\mathbf{v}^x_{i+1/2,j,k} - \mathbf{v}^x_{i-1/2,j,k}}{h} + \frac{\mathbf{v}^y_{i,j+1/2,k} - \mathbf{v}^y_{i,j-1/2,k}}{h} + \frac{\mathbf{v}^z_{i,j,k+1/2} - \mathbf{v}^z_{i,j,k-1/2}}{h} \tag{155}$$

The components $\mathbf{v}^x$, $\mathbf{v}^y$, and $\mathbf{v}^x$ are scalar products of the vector field $\mathbf{v}$ with respective unit normal vectors. One can demonstrated that at the cell center Equation (155) approximates the divergence of smooth vector field v to the second-order accuracy.

Combining Equations (150) and (155), one obtains

$$\begin{aligned}\nabla \cdot (K \nabla p) \approx {} & \frac{(K\nabla p)^x_{i+1/2,j,k} - (K\nabla p)^x_{i-1/2,j,k}}{h} \\ & + \frac{(K\nabla p)^y_{i,j+1/2,k} - (K\nabla p)^y_{i,j-1/2,k}}{h} + \frac{(K\nabla p)^z_{i,j,k+1/2} - (K\nabla p)^z_{i,j,k-1/2}}{h}\end{aligned} \tag{156}$$

A substitution of expressions (150) yields

$$\begin{aligned}
\nabla \cdot (K\nabla p) \approx {} & \frac{1}{h^2}\left\{\left[\frac{1}{2}\left(K^{-1}_{i,j,k} + K^{-1}_{i+1,j,k}\right)\right]^{-1}\right\}^x \cdot \begin{pmatrix} p_{i+1,j,k} - p_{i,j,k} \\ \frac{p_{i+1,j+1,k} + p_{i,j+1,k}}{4} - \frac{p_{i+1,j-1,k} + p_{i,j-1,k}}{4} \\ \frac{p_{i+1,j,k+1} + p_{i,j,k+1}}{4} - \frac{p_{i+1,j,k-1} + p_{i,j,k-1}}{4} \end{pmatrix} \\
& - \frac{1}{h^2}\left\{\left[\frac{1}{2}\left(K^{-1}_{i-1,j,k} + K^{-1}_{i,j,k}\right)\right]^{-1}\right\}^x \cdot \begin{pmatrix} p_{i,j,k} - p_{i-1,j,k} \\ \frac{p_{i,j+1,k} + p_{i-1,j+1,k}}{4} - \frac{p_{i,j-1,k} + p_{i-1,j-1,k}}{4} \\ \frac{p_{i,j,k+1} + p_{i-1,j,k+1}}{4} - \frac{p_{i,j,k-1} + p_{i-1,j,k-1}}{4} \end{pmatrix} \\
& + \frac{1}{h^2}\left\{\left[\frac{1}{2}\left(K^{-1}_{i,j,k} + K^{-1}_{i,j+1,k}\right)\right]^{-1}\right\}^y \cdot \begin{pmatrix} \frac{p_{i+1,j+1,k} + p_{i+1,j,k}}{4} - \frac{p_{i-1,j+1,k} + p_{i-1,j,k}}{4} \\ p_{i,j+1,k} - p_{i,j,k} \\ \frac{p_{i,j+1,k+1} + p_{i,j,k+1}}{4} - \frac{p_{i,j+1,k-1} + p_{i,j,k-1}}{4} \end{pmatrix} \\
& - \frac{1}{h^2}\left\{\left[\frac{1}{2}\left(K^{-1}_{i,j-1,k} + K^{-1}_{i,j,k}\right)\right]^{-1}\right\}^y \cdot \begin{pmatrix} \frac{p_{i+1,j,k} + p_{i+1,j-1,k}}{4} - \frac{p_{i-1,j,k} + p_{i-1,j-1,k}}{4} \\ p_{i,j,k} - p_{i,j-1,k} \\ \frac{p_{i,j,k+1} + p_{i,j-1,k+1}}{4} - \frac{p_{i,j,k-1} + p_{i,j-1,k-1}}{4} \end{pmatrix} \\
& + \frac{1}{h^2}\left\{\left[\frac{1}{2}\left(K^{-1}_{i,j,k} + K^{-1}_{i,j,k+1}\right)\right]^{-1}\right\}^z \cdot \begin{pmatrix} \frac{p_{i+1,j,k+1} + p_{i+1,j,k}}{4} - \frac{p_{i-1,j,k+1} + p_{i-1,j,k}}{4} \\ \frac{p_{i,j+1,k+1} + p_{i,j+1,k}}{4} - \frac{p_{i,j-1,k+1} + p_{i,j-1,k}}{4} \\ p_{i,j,k+1} - p_{i,j,k} \end{pmatrix} \\
& - \frac{1}{h^2}\left\{\left[\frac{1}{2}\left(K^{-1}_{i,j,k-1} + K^{-1}_{i,j,k}\right)\right]^{-1}\right\}^z \cdot \begin{pmatrix} \frac{p_{i+1,j,k} + p_{i+1,j,k-1}}{4} - \frac{p_{i-1,j,k} + p_{i-1,j,k-1}}{4} \\ \frac{p_{i,j+1,k} + p_{i,j+1,k-1}}{4} - \frac{p_{i,j-1,k} + p_{i,j-1,k-1}}{4} \\ p_{i,j,k} - p_{i,j,k-1} \end{pmatrix}
\end{aligned} \tag{157}$$

Equivalently, one can write:

$$\begin{aligned}
\nabla\cdot(K\nabla p) \approx D_{0,0,0}p_{i,j,k} &+ D_{-1,-1,0}p_{i-1,j-1,k} + D_{-1,0,-1}p_{i-1,j,k-1} + D_{0,-1,-1}p_{i,j-1,k-1}\\
&+ D_{-1,1,0}p_{i-1,j+1,k} + D_{-1,0,1}p_{i-1,j,k+1} + D_{0,-1,1}p_{i,j-1,k+1}\\
&+ D_{1,-1,0}p_{i+1,j-1,k} + D_{1,0,-1}p_{i+1,j,k-1} + D_{0,1,-1}p_{i,j+1,k-1}\\
&+ D_{1,1,0}p_{i+1,j+1,k} + D_{1,0,1}p_{i+1,j,k+1} + D_{0,1,1}p_{i,j+1,k+1}\\
&+ D_{-1,0,0}p_{i-1,j,k} + D_{0,-1,0}p_{i,j-1,k} + D_{0,0,-1}p_{i,j,k-1}\\
&+ D_{1,0,0}p_{i+1,j,k} + D_{0,1,0}p_{i,j+1,k} + D_{0,0,1}p_{i,j,k+1}
\end{aligned} \tag{158}$$

Equation (150) yields the following expressions for the coefficients D:

$$\begin{aligned}
D_{0,0,0} =& -\frac{1}{h^2}\left\{\left[\frac{1}{2}\left(K^{-1}_{i,j,k}+K^{-1}_{i+1,j,k}\right)\right]^{-1}+\left[\frac{1}{2}\left(K^{-1}_{i,j,k}+K^{-1}_{i-1,j,k}\right)\right]^{-1}\right\}^x_1\\
&+\frac{1}{h^2}\left\{\left[\frac{1}{2}\left(K^{-1}_{i,j,k}+K^{-1}_{i,j+1,k}\right)\right]^{-1}+\left[\frac{1}{2}\left(K^{-1}_{i,j,k}+K^{-1}_{i,j-1,k}\right)\right]^{-1}\right\}^y_2\\
&+\frac{1}{h^2}\left\{\left[\frac{1}{2}\left(K^{-1}_{i,j,k}+K^{-1}_{i,j,k+1}\right)\right]^{-1}+\left[\frac{1}{2}\left(K^{-1}_{i,j,k}+K^{-1}_{i,j,k-1}\right)\right]^{-1}\right\}^z_3
\end{aligned}$$

$$\begin{aligned}
D_{-1,0,0} =& \frac{1}{h^2}\left\{\left[\frac{1}{2}\left(K^{-1}_{i-1,j,k}+K^{-1}_{i,j,k}\right)\right]^{-1}\right\}^x_1\\
&-\frac{1}{4h^2}\left\{\left[\frac{1}{2}\left(K^{-1}_{i,j,k}+K^{-1}_{i,j+1,k}\right)\right]^{-1}\right\}^y_1+\frac{1}{4h^2}\left\{\left[\frac{1}{2}\left(K^{-1}_{i,j-1,k}+K^{-1}_{i,j,k}\right)\right]^{-1}\right\}^y_1\\
&-\frac{1}{4h^2}\left\{\left[\frac{1}{2}\left(K^{-1}_{i,j,k}+K^{-1}_{i,j,k+1}\right)\right]^{-1}\right\}^z_1+\frac{1}{4h^2}\left\{\left[\frac{1}{2}\left(K^{-1}_{i,j,k-1}+K^{-1}_{i,j,k}\right)\right]^{-1}\right\}^z_1\\
D_{0,-1,0} =& -\frac{1}{4h^2}\left\{\left[\frac{1}{2}\left(K^{-1}_{i-1,j,k}+K^{-1}_{i,j,k}\right)\right]^{-1}\right\}^x_2+\frac{1}{4h^2}\left\{\left[\frac{1}{2}\left(K^{-1}_{i,j,k}+K^{-1}_{i+1,j,k}\right)\right]^{-1}\right\}^x_2\\
&+\frac{1}{h^2}\left\{\left[\frac{1}{2}\left(K^{-1}_{i,j-1,k}+K^{-1}_{i,j,k}\right)\right]^{-1}\right\}^y_2\\
&-\frac{1}{4h^2}\left\{\left[\frac{1}{2}\left(K^{-1}_{i,j,k}+K^{-1}_{i,j,k+1}\right)\right]^{-1}\right\}^z_2+\frac{1}{4h^2}\left\{\left[\frac{1}{2}\left(K^{-1}_{i,j,k-1}+K^{-1}_{i,j,k}\right)\right]^{-1}\right\}^z_2\\
D_{0,0,-1} =& -\frac{1}{4h^2}\left\{\left[\frac{1}{2}\left(K^{-1}_{i-1,j,k}+K^{-1}_{i,j,k}\right)\right]^{-1}\right\}^x_3+\frac{1}{4h^2}\left\{\left[\frac{1}{2}\left(K^{-1}_{i,j,k}+K^{-1}_{i+1,j,k}\right)\right]^{-1}\right\}^x_3\\
&-\frac{1}{4h^2}\left\{\left[\frac{1}{2}\left(K^{-1}_{i,j,k}+K^{-1}_{i,j+1,k}\right)\right]^{-1}\right\}^y_3+\frac{1}{4h^2}\left\{\left[\frac{1}{2}\left(K^{-1}_{i,j-1,k}+K^{-1}_{i,j,k}\right)\right]^{-1}\right\}^y_3\\
&+\frac{1}{h^2}\left\{\left[\frac{1}{2}\left(K^{-1}_{i,j,k-1}+K^{-1}_{i,j,k}\right)\right]^{-1}\right\}^z_3\\
D_{1,0,0} =& \frac{1}{h^2}\left\{\left[\frac{1}{2}\left(K^{-1}_{i,j,k}+K^{-1}_{i+1,j,k}\right)\right]^{-1}\right\}^x_1
\end{aligned}$$

$$\begin{aligned}
&+\frac{1}{4h^2}\left\{\left[\frac{1}{2}\left(K^{-1}_{i,j,k}+K^{-1}_{i,j+1,k}\right)\right]^{-1}\right\}^{y}_{1}-\frac{1}{4h^2}\left\{\left[\frac{1}{2}\left(K^{-1}_{i,j-1,k}+K^{-1}_{i,j,k}\right)\right]^{-1}\right\}^{y}_{1}\\
&+\frac{1}{4h^2}\left\{\left[\frac{1}{2}\left(K^{-1}_{i,j,k}+K^{-1}_{i,j,k+1}\right)\right]^{-1}\right\}^{z}_{1}-\frac{1}{4h^2}\left\{\left[\frac{1}{2}\left(K^{-1}_{i,j,k-1}+K^{-1}_{i,j,k}\right)\right]^{-1}\right\}^{z}_{1}\\
D_{0,1,0}=&\frac{1}{4h^2}\left\{\left[\frac{1}{2}\left(K^{-1}_{i-1,j,k}+K^{-1}_{i,j,k}\right)\right]^{-1}\right\}^{x}_{2}-\frac{1}{4h^2}\left\{\left[\frac{1}{2}\left(K^{-1}_{i,j,k}+K^{-1}_{i+1,j,k}\right)\right]^{-1}\right\}^{x}_{2}\\
&+\frac{1}{h^2}\left\{\left[\frac{1}{2}\left(K^{-1}_{i,j-1,k}+K^{-1}_{i,j,k}\right)\right]^{-1}\right\}^{y}_{2}\\
&+\frac{1}{4h^2}\left\{\left[\frac{1}{2}\left(K^{-1}_{i,j,k}+K^{-1}_{i,j,k+1}\right)\right]^{-1}\right\}^{z}_{2}-\frac{1}{4h^2}\left\{\left[\frac{1}{2}\left(K^{-1}_{i,j,k-1}+K^{-1}_{i,j,k}\right)\right]^{-1}\right\}^{z}_{2}\\
D_{0,0,1}=&\frac{1}{4h^2}\left\{\left[\frac{1}{2}\left(K^{-1}_{i-1,j,k}+K^{-1}_{i,j,k}\right)\right]^{-1}\right\}^{x}_{3}-\frac{1}{4h^2}\left\{\left[\frac{1}{2}\left(K^{-1}_{i,j,k}+K^{-1}_{i+1,j,k}\right)\right]^{-1}\right\}^{x}_{3}\\
&+\frac{1}{4h^2}\left\{\left[\frac{1}{2}\left(K^{-1}_{i,j,k}+K^{-1}_{i,j+1,k}\right)\right]^{-1}\right\}^{y}_{3}-\frac{1}{4h^2}\left\{\left[\frac{1}{2}\left(K^{-1}_{i,j-1,k}+K^{-1}_{i,j,k}\right)\right]^{-1}\right\}^{y}_{3}\\
&+\frac{1}{h^2}\left\{\left[\frac{1}{2}\left(K^{-1}_{i,j,k}+K^{-1}_{i,j,k+1}\right)\right]^{-1}\right\}^{z}_{3}
\end{aligned}$$

and

$$\begin{aligned}
D_{-1,-1,0}=&\frac{1}{4h^2}\left\{\left[\frac{1}{2}\left(K^{-1}_{i-1,j,k}+K^{-1}_{i,j,k}\right)\right]^{-1}\right\}^{x}_{2}+\frac{1}{4h^2}\left\{\left[\frac{1}{2}\left(K^{-1}_{i,j-1,k}+K^{-1}_{i,j,k}\right)\right]^{-1}\right\}^{y}_{1}\\
D_{-1,1,0}=&-\frac{1}{4h^2}\left\{\left[\frac{1}{2}\left(K^{-1}_{i-1,j,k}+K^{-1}_{i,j,k}\right)\right]^{-1}\right\}^{x}_{2}-\frac{1}{4h^2}\left\{\left[\frac{1}{2}\left(K^{-1}_{i,j,k}+K^{-1}_{i,j+1,k}\right)\right]^{-1}\right\}^{y}_{1}\\
D_{1,-1,0}=&-\frac{1}{4h^2}\left\{\left[\frac{1}{2}\left(K^{-1}_{i,j,k}+K^{-1}_{i+1,j,k}\right)\right]^{-1}\right\}^{x}_{2}-\frac{1}{4h^2}\left\{\left[\frac{1}{2}\left(K^{-1}_{i,j-1,k}+K^{-1}_{i,j,k}\right)\right]^{-1}\right\}^{y}_{1}\\
D_{-1,0,-1}=&\frac{1}{4h^2}\left\{\left[\frac{1}{2}\left(K^{-1}_{i-1,j,k}+K^{-1}_{i,j,k}\right)\right]^{-1}\right\}^{x}_{3}+\frac{1}{4h^2}\left\{\left[\frac{1}{2}\left(K^{-1}_{i,j,k-1}+K^{-1}_{i,j,k}\right)\right]^{-1}\right\}^{z}_{1}\\
D_{-1,0,1}=&-\frac{1}{4h^2}\left\{\left[\frac{1}{2}\left(K^{-1}_{i-1,j,k}+K^{-1}_{i,j,k}\right)\right]^{-1}\right\}^{x}_{3}-\frac{1}{4h^2}\left\{\left[\frac{1}{2}\left(K^{-1}_{i,j,k}+K^{-1}_{i,j,k+1}\right)\right]^{-1}\right\}^{z}_{1}\\
D_{1,0,-1}=&-\frac{1}{4h^2}\left\{\left[\frac{1}{2}\left(K^{-1}_{i,j,k}+K^{-1}_{i+1,j,k}\right)\right]^{-1}\right\}^{x}_{3}-\frac{1}{4h^2}\left\{\left[\frac{1}{2}\left(K^{-1}_{i,j,k-1}+K^{-1}_{i,j,k}\right)\right]^{-1}\right\}^{z}_{1}\\
D_{0,-1,-1}=&\frac{1}{4h^2}\left\{\left[\frac{1}{2}\left(K^{-1}_{i,j-1,k}+K^{-1}_{i,j,k}\right)\right]^{-1}\right\}^{y}_{3}+\frac{1}{4h^2}\left\{\left[\frac{1}{2}\left(K^{-1}_{i,j,k-1}+K^{-1}_{i,j,k}\right)\right]^{-1}\right\}^{z}_{2}\\
D_{0,-1,1}=&-\frac{1}{4h^2}\left\{\left[\frac{1}{2}\left(K^{-1}_{i,j-1,k}+K^{-1}_{i,j,k}\right)\right]^{-1}\right\}^{y}_{3}-\frac{1}{4h^2}\left\{\left[\frac{1}{2}\left(K^{-1}_{i,j,k}+K^{-1}_{i,j,k+1}\right)\right]^{-1}\right\}^{z}_{2}
\end{aligned}$$

$$\begin{aligned}
D_{0,1,-1} &= -\frac{1}{4h^2}\left\{\left[\frac{1}{2}\left(K^{-1}_{i,j-1,k}+K^{-1}_{i,j+1,k}\right)\right]^{-1}\right\}^{y}_{3} - \frac{1}{4h^2}\left\{\left[\frac{1}{2}\left(K^{-1}_{i,j,k-1}+K^{-1}_{i,j,k}\right)\right]^{-1}\right\}^{z}_{2}\\
D_{1,1,0} &= \frac{1}{4h^2}\left\{\left[\frac{1}{2}\left(K^{-1}_{i,j,k}+K^{-1}_{i+1,j,k}\right)\right]^{-1}\right\}^{x}_{2} + \frac{1}{4h^2}\left\{\left[\frac{1}{2}\left(K^{-1}_{i,j,k}+K^{-1}_{i,j+1,k}\right)\right]^{-1}\right\}^{y}_{1}\\
D_{1,0,1} &= \frac{1}{4h^2}\left\{\left[\frac{1}{2}\left(K^{-1}_{i,j,k}+K^{-1}_{i+1,j,k}\right)\right]^{-1}\right\}^{x}_{3} + \frac{1}{4h^2}\left\{\left[\frac{1}{2}\left(K^{-1}_{i,j,k}+K^{-1}_{i,j,k+1}\right)\right]^{-1}\right\}^{z}_{1}\\
D_{0,1,1} &= \frac{1}{4h^2}\left\{\left[\frac{1}{2}\left(K^{-1}_{i,j,k}+K^{-1}_{i,j+1,k}\right)\right]^{-1}\right\}^{y}_{3} + \frac{1}{4h^2}\left\{\left[\frac{1}{2}\left(K^{-1}_{i,j,k}+K^{-1}_{i,j,k+1}\right)\right]^{-1}\right\}^{z}_{2}
\end{aligned}$$

7. COMPUTER MODELS OF SAND AND TIGHT SAND

Alternatively to imaging, digital data can be generated in a computer. The advantage of this approach is that the data can be digitized at an arbitrary high resolution. This approach is much less time consuming than any imaging technique. Generating data in computer does not require expensive tools. Segmentation of tomography data always involves uncertainty, the best segmentation algorithm simply does not yet exist [32, 56]. Computer-generated images discussed in this section are binary by their nature, so the segmentation process is straightforward. At the same time, working with computer-generated data introduces the risk of loosening the contact with reality, so one has proceed with caution.

7.1. **Modeling granular media.** The procedure proposed here relies on three main components. First, the coordinates of future grain centers have to be generated. We utilize the centers of a pack of spherical grains computed by simulation of compaction [31]. Second, the initial grain structures are generated by Voronoi tesselation [3, 74]. A number of tesselation algorithms are known. This study used the open-source package Quickhull [6]. The output of this algorithm can be interpreted as a zero-porosity pack of angular grains, where each grain is a convex body described by a number of linear inequalities. On the last step, the grains are shrunk and rotated to develop porosity. Additionally, some grains can be generated besides tesselation and inserted into the pores for modeling microporosity. A fracture can be modeled by parting grains along a plane.

Figure 39 shows an example of granular structure generated by the algorithm described above, and micro CT data of Bentheimer sandstone. The dark areas in the microtomography data correspond to the exposures of pores. In the computer-generated medium, the pores are transparent. The computed sample is visually similar to Bentheimer. The porosity of computer-generated sample is 22 %, whereas the sandstone sample porosity is estimated at 20 %. Ineterstingly, even though the resolution of the "virtual rock" image is almost twice coarser than that of the sandstone, the dimensionless capillary pressure curves are close to each other, see Figure 40. The curves were computed using the method of Maximal Inscribed Spheres [59, 65, 70] for two contact angles: 0 ° and 45 °.

The pores in tight-sand samples are partially filled with clay, which creates microporosity [63, 64]. The SEM images in Figure 41 show various types of clay at grain surfaces. Microporosity associated with these clay structures affects flow properties of the rock and has to be incorporated into the idealized model of the rock described above. To model microporosity, we generate clusters of grains of special form that mimic clay structures. Figure 42 shows two examples of computer-generated structures mimicking clay fillings shown in Figure 41. The structure in exhibit (a) was generated by translation and rotation of two hexagonal plates. To generate structure (b), the plates were rotated in space by random angles.

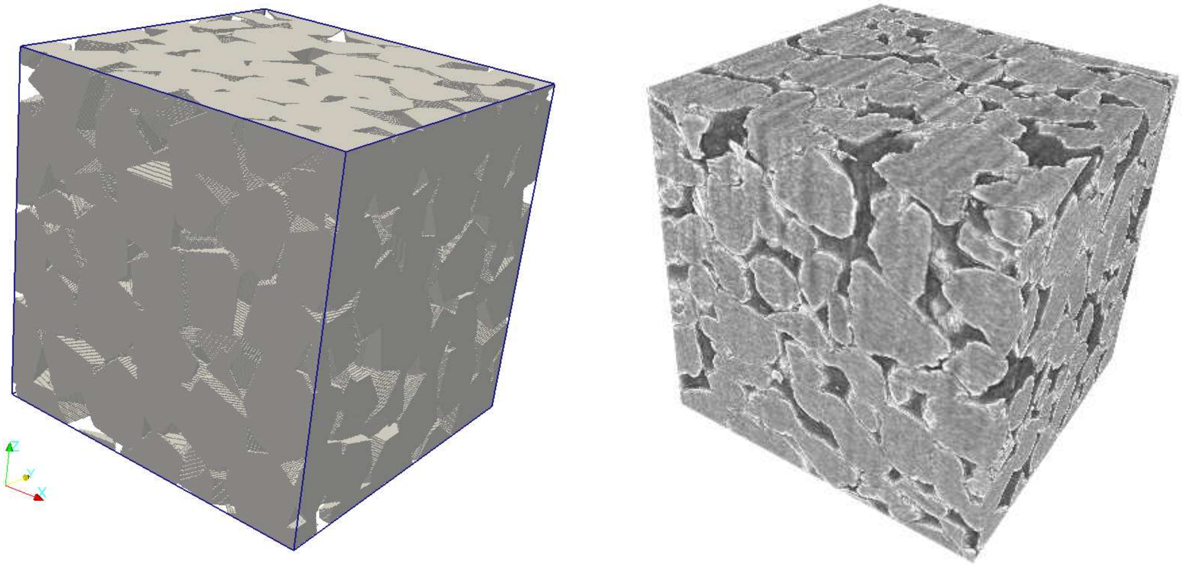

Figure 39. Digitized computer-generated porous structure, on the left, and gray-scale micro CT data for a sample of Bentheimer sandstone with voxel size 4.42 μm, on the right.

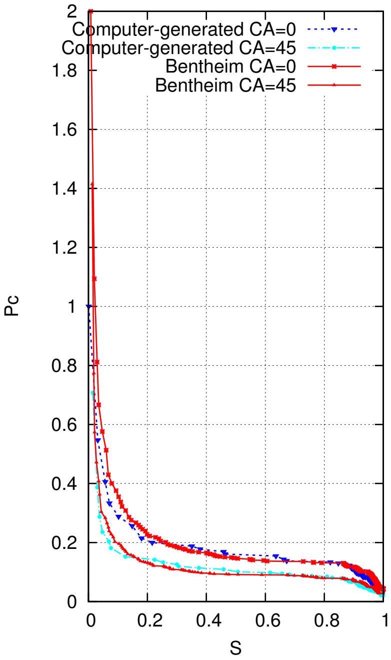

Figure 40. Dimensionless capillary pressure evaluated from images of computer-generated and natural rock samples for two different contact angles (CA).

7.2. **Modeling tight rock with slit-like pores.** Micro CT images of some samples show very narrow slit-like pores. Due to limitations of the imaging tools, the image resolution is insufficient for generating binary data suitable for numerical simulations [64, Figure 10]. Computer-generated structures shown in Figure 43 was obtained using the procedure described above with small random

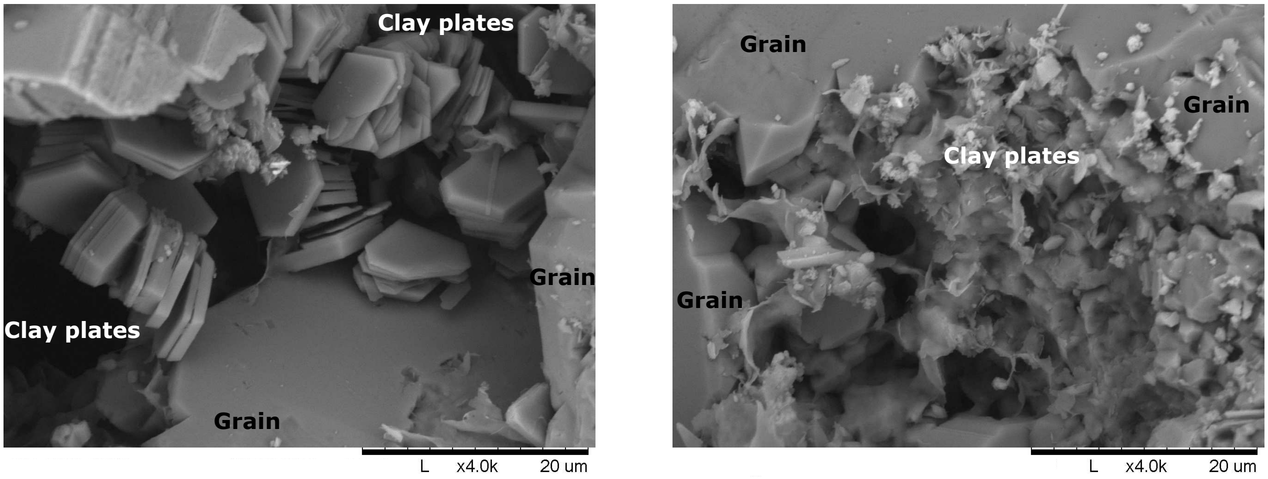

(a) (b)

FIGURE 41. SEM 4000× magnification images show different types of clay plates contribute to the microporosity of the sample: kaolinite (a) and montmorillonite (b).

(a) (b)

FIGURE 42. Computer-generated structures to mimic pore fillings by clay, *cf* Figure 41.

rotations and only slight shrinking of the grains. The same medium can model a fractured rock with low-permeability blocks and connected network of fractures.

The images were digitized at two resolutions producing two data sets: 250 × 250 × 250 and 500 × 500 × 500 voxels. Figure 44 shows drainage capillary pressure curves evaluated for two contact angles for both resolutions by the method of maximal inscribed spheres. The curves are dimensionless. They data can be easily transformed into physically meaningful units by applying scaling factor accounting for the interfacial tension and voxel size. For instance, for a surface tension coefficient of 0.07 N/m and voxel size 0.1 μm, a multiplication of the dimensionless pressures by 700 will produce capillary pressure in kPa.

Figure 45 show relative permeability curves evaluated for the medium shown in Figure 43. For mixed-wet environment, simulations produce relative permeability curve resembling straight lines. The intersection of the curves for mixed-wet environment is around a common relative permeability value of 0.1, which is almost twice higher than the respective value for the wet environment. A distinctive feature of the plots in Figure 45 is that the drainage and imbibition curves almost coincide. The above-zero intersection of the plots in Figure 45 makes them different from the computed relative permeability curves reported in [64]. The latter means that the permeability jail phenomenon [15, 57] is pertinent to matrix porosity and is less likely to occur in fractures.

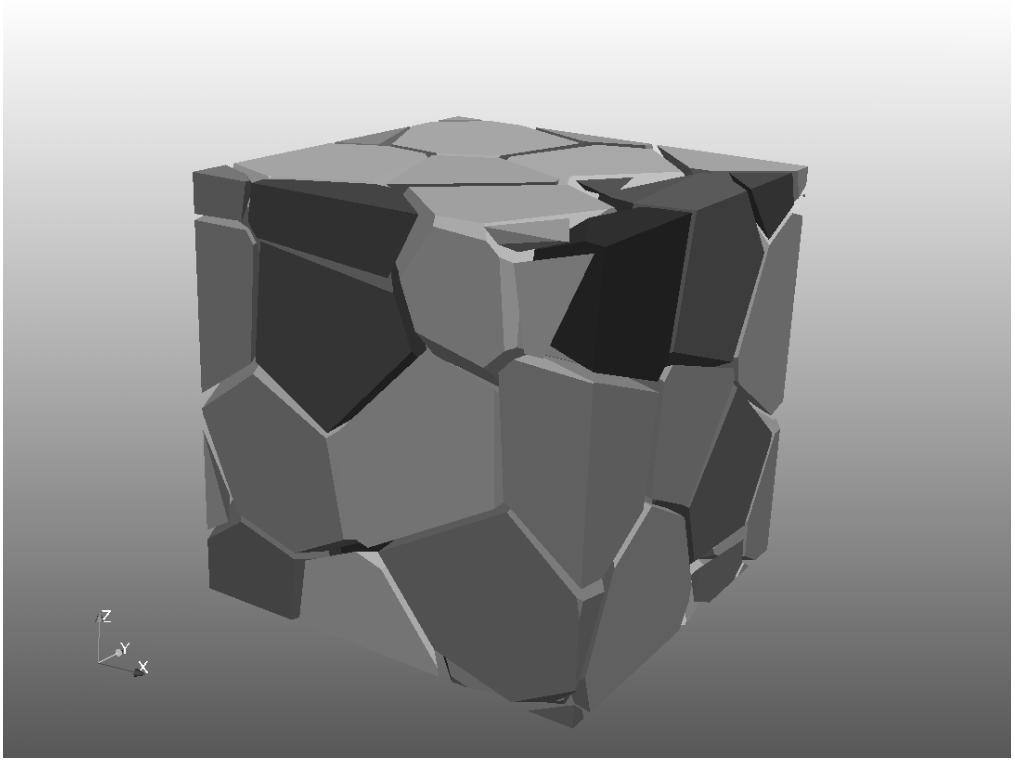

Figure 43. Computer-generated structure with slit-like narrow pores

7.3. **Numerical evaluation of permeability with slippage.** Figure 46 shows results of flow simulation with slippage boundary conditions, as described in Section 4.2. The input data were computer-generated samples: a sample mimicking sandstone with crack, a sample modeling sandstone matrix, and a sample with slit-like pores, or fractures. The results show that the dependence of the permeability on slippage factor is qualitatively similar in all situations. The sample with crack, though shows slow permeability increment. The distinctive feature of this sample relative to the other two is permeability contrast: fracture carries most of fluid flow. Unlike flow in simple-geometry channels, where the correlation between the flux and slippage is linear (see Equations (24) and (28)), the computations predict nonlinear dependence of the permeability on slippage.

The slippage coefficient G is defined in Equation (17). It has the dimensionality of length. An accurate evaluation of this coefficient in specific physical conditions needs further study. The developed algorithms are ready to accommodate the specific value of G as input parameter.

8. Summary and conclusions

This study focuses on a number of computer-assisted methods of evaluating rock flow properties. The approaches discussed here are based on direct analysis of the 3D data, without resorting to simplified representation of the pore space as a network of channels. The input data can be a segmented 3D computed-tomography image, or computer-generated digital data mimicking natural rock. The permeability can be estimated by averaging local flow velocities of viscous flow at zero Reynolds number. The developed tools allow for flow simulations with no-slip or slippage boundary conditions. Codes and algorithms for numerical evaluation of permeability were a big part of this study. The advantage of the method of finite differences relative to alternative approaches is its rigorous handling of boundary conditions. This circumstance was the principal reason of employing this method in the present study. The objective of presenting equations in full detail was to

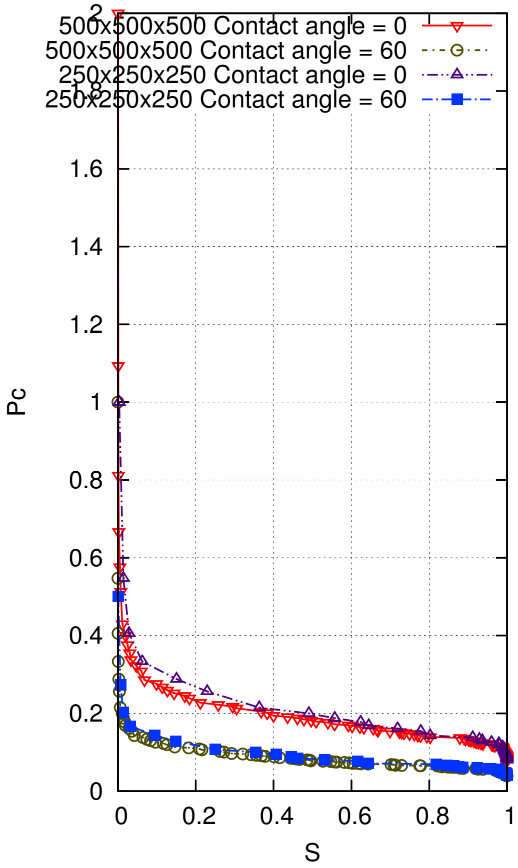

Figure 44. Dimensionless capillary pressure curves computed for different resolutions and two contact angles

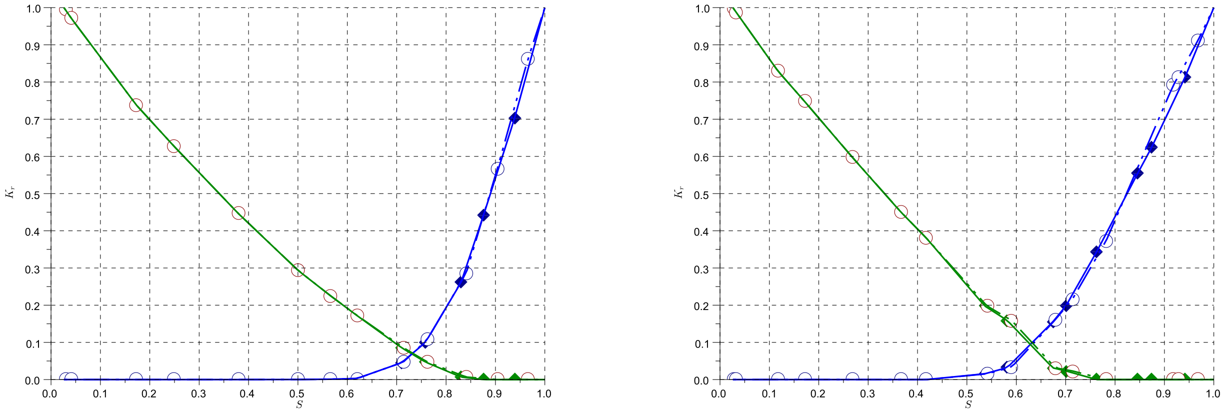

(a) (b)

Figure 45. Relative permeability curves evaluated for media with slit-like pores evaluated for zero, (a), and 60°, (b), contact angles.

provide computational formulas ready for incorporation into computer codes. Numerical examples demonstrate feasibility and functionality of such codes implemented in C++.

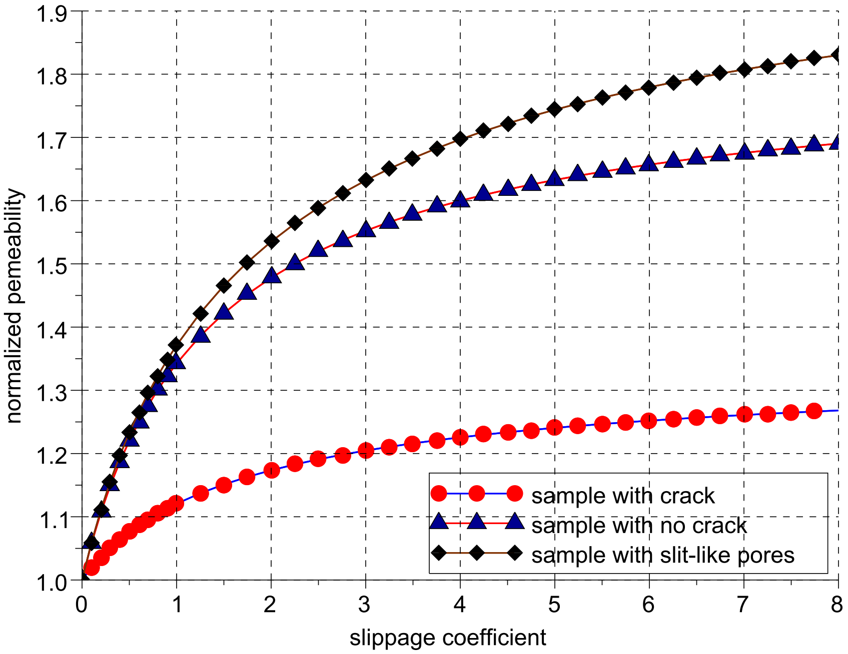

FIGURE 46. Estimated permeability versus slippage coeffcient. The permeability is normalized with no-slip flow.

Employment of a matrix preconditioner makes the linear solver more robust and efficient, but complicates massive parallelization of the computations. Thus, evaluation of permeability on a large data set is a very demanding task. As a workaround of this limitation, a large data set can be partitioned into subsamples of relatively small size. On each part, the permeability tensor is evaluated by solving a reasonably small boundary-value problem for Stokes equations. This part of the procedure is embarrassingly parallel since it consists of a number of mutually independent tasks. However, it has to be complemented by an averaging algorithm computing the permeability of the large data set. It is not uncommon that the permeability of each small subsample needs to be characterized by a full tensor, rather than single coefficient. Thus, a discretization scheme and algorithms have been developed to handle upscaling of full-tensor subsample permeabilities to the permeability of the entire image. The input data of this upscaling procedure is a 3D grid of blocks with individual permeability tensors. It turns out that an unbiased random distribution of permeability tensor usually upscales to a scalar permeability. This, the small-sample anisotropy is not necessarily a manifestation of physical anisotropy of the rock, but can be a consequence of the scale only.

For two-phase flow simulations, the proposed method has to be combined with the maximal inscribed spheres procedure. MIS calculations produce fluid distribution in capillary equilibrium. Evaluation of the permeability of the portion of the pore space occupied by each fluid phase, and scaling this estimate with the evaluated absolute permeability leads to computed relative permeability curves. Additional connectivity analysis makes possible evaluation of relative permeability for various fluid displacement scenarios. For example, fluid distribution based on ordinary percolation algorithms does not account for the flow path of each phase and is more suitable for estimating relative permeability curves for liquid dropout or gas exsolution. The invasion-percolation algorithms create nonwetting fluid distributions always connected to the sample boundaries, and is suitable for simulating drainage. These two examples cannot cover the enormous variety of different fluid displacement scenarios.

Computer models of natural rock were used to mimic natural rocks for which extraction of binary digital data from microtomography images was difficult due to the resolution limitations of imaging tools. In this study, the focus was on sandstone with slit-like pores. The model mimicking rock geometry employs QuickHull algorithm and uses the centers of spheres computed by a depositional model as input data. The good agreement between capillary pressure curves evaluated for computer-generated and micro CT data at different contact angles confirmed the validity of the approach. Evaluation of relative permeability curves for a computer-generated structure with slit-like pores showed that the phase permeability curves intersect at a nonzero value of permeability. It means that at least one fluid phase remains mobile in the entire range of saturation. It is known that in tight sands it may be not true due to the permeability jail effect.

To summarize,this report has considered just a few digital rock tools and approaches to studying flow phenomena in tight rocks. Future development will lead to a more comprehensive understanding of tight rocks that will help to produce unconventional energy reserves more efficiently and in environmentally safe manner.

9. Acknowledgments

This work has been performed at Lawrence Berkeley National Laboratory (LBNL) of the U.S. Department of Energy (DOE) under Contract No. DE-AC02-05CH11231. Funding for this project is provided by Research Partnership to Secure Energy for America (RPSEA) through the Ultra-Deepwater and Unconventional Natural Gas and Other Petroleum Resources program authorized by the U.S. Energy Policy Act of 2005. RPSEA (www.rpsea.org) is a nonprofit corporation whose mission is to provide a stewardship role in ensuring the focused research, development and deployment of safe and environmentally responsible technology that can effectively deliver hydrocarbons from domestic resources to the citizens of the United States. RPSEA, operating as a consortium of premier U.S. energy research universities, industry, and independent research organizations, manages the program under a contract with the U.S. DOE's National Energy Technology Laboratory. Partial support was provided by the Research Council of Norway, ConocoPhillips and the Ekofisk co-venturers, including TOTAL, ENI, Statoil and Petoro through a contract with the International Research Institute of Stavanger.

References

1. W. G. Anderson, *Wettability literature survey– Part 1: Rock/oi/brine interactions and the effects of core handling on wettabiiity*, Journal of Petroleum Technology **38** (1986), 1125–1144.
2. ———, *Wettability literature survey– Part 4: Effects of wettability on capillary pressure*, Journal of Petroleum Technology **39** (1987), no. 10, 1283–1300.
3. Franz Aurenhammer, *Voronoi diagrams — a survey of a fundamental geometric data structure*, ACM Comput. Surv. **23** (1991), no. 3, 345–405.
4. F. M. Auzerais, J. Dunsmuir, B. B. Ferreol, N. Martys, J. Olson, T. S. Ramakrishnan, D. H. Rothman, and L. M. Schwartz, *Transport in sandstone: A study based on three dimensional microtomography*, Geophysycal Research Letters **23** (1996), 705–708.
5. S. Bakke and P. E. Øren, *3-D pore-scale modeling of sandstones and flow simulations in the pore networks*, SPE Journal **2** (1997), 136–149.
6. C. B. Barber, D. P. Dobkin, and H. T. Huhdanpaa, *The Quickhull algorithm for convex hulls*, ACM Trans. on Mathematical Software **22** (1996), 469–483.
7. Robert W. Barber and David R. Emerson, *Challenges in modeling gas-phase flow in microchannels: From slip to transition*, Heat Transfer Engineering **27** (2006), no. 4, 3–12.

8. M. J. Blunt, *Flow in porous media - pore-network models and multiphase flow*, Current Opinion in Colloid & Interface Science **6** (2001), no. 3, 197–207.
9. Stephen Brunauer, Lola S. Deming, W. Edwards Deming, and Edward Teller, *On a theory of the van der Waals adsorption of gases*, Journal of the American Chemical Society **62** (1940), no. 7, 1723–1732.
10. Stephen Brunauer, P. H. Emmett, and Edward Teller, *Adsorption of gases in multimolecular layers*, Journal of the American Chemical Society **60** (1938), no. 2, 309–319.
11. D. Burnett, *The distribution of molecular velocities and the mean motion in a non-uniform gas*, Proc. London Math. Soc. **40** (1936), 382–435.
12. A. J. Chorin, *A numerical method for solving incompressible viscous flow problems*, Journal of Computational Physics **2** (1967), 12–26.
13. ______, *Numerical solution of the Navier–Stokes equations*, Math. Comp. **22** (1968), 745–762.
14. Faruk Civan, Chandra Rai, and Carl Sondergeld, *Shale-gas permeability and diffusivity inferred by improved formulation of relevant retention and transport mechanisms*, Transport in Porous Media **86** (2011), 925–944, 10.1007/s11242-010-9665-x.
15. Robert M. Cluff and Alan P. Byrnes, *Relative permeability in tight gas sandstone reservoirs – the "Permeability Jail" model*, SPWLA 51st Annual Logging Symposium, June 19-23, 2010.
16. M. E. Coles, R. D. Hazlett, P. Spanne, E. L. Muegge, and M. J. Furr, *Characterization of reservoir core using computed microtomography*, SPE Journal **1** (1996), no. 3, 295–302.
17. P.-G. de Gennes, *Wetting: statics and dynamics*, Reviewes of Modern Physics **57** (1985), no. 3, 827–863.
18. R. G. Deissler, *An analysis of second-order slip flow and temperature-jump boundary conditions for rarefied gases*, Journal of Heat and Mass Transfer **7** (1964), 681–694.
19. Jack Dongarra, Andrew Lumsdaine, Xinhiu Niu, Pozo Roldan, and Karin Remington, *A sparse matrix library in C++ for high performance architectures*, Proceedings of the Second Object Oriented Numerics Conference, 1994.
20. M. D. Donohue and G. L. Aranovich, *Adsorption hysteresis in porous solids*, Journal of Colloid and Interface Science **205** (1998), no. 1, 121 – 130.
21. M. M. Dubinin, *The potential theory of adsorption of gases and vapors for adsorbents with energetically nonuniform surfaces.*, Chemical Reviews **60** (1960), no. 2, 235–241.
22. V. M. Entov, *The micromechanics of flow in porous media*, Soviet Academy Izvestia. Mechanics of Gas and Fluids (1992), no. 6, 90–102.
23. Turgay Ertekin, Gregory R. King, and Fred C. Schvwerer, *Dynamic gas slippage: A unique dual-mechanism approach to the flow of gas in tight formations*, SPE Formation Evaluation (1986), 43–52.
24. I. Fatt, *The network model of porous media. 1. Capillary pressure characteristics*, Trans. AIME **207** (1956), no. 7, 144–159.
25. A. P. Favorskii, A. A. Samarskii, M. Yu. Shashkov, and V. F. Tishkin, *Operational finite-difference schemes*, Differential Equations **17** (1981), 854.
26. J. T. Fredrich and R. M. O'Connor, *Microscale flow modeling in reconstructed porous media*, Trans. American Geophysical Union. (1998).
27. Sebastian Geller, Manfred Krafczyk, Jonas Tölke, Stefan Turek, and Jaroslav Hron, *Benchmark computations based on lattice-Boltzmann, finite element and finite volume methods for laminar flows*, Computers & Fluids **35** (2006), no. 8-9, 888–897, Proceedings of the First International Conference for Mesoscopic Methods in Engineering and Science.
28. F.H. Harlow and J.E. Welsh, *Numerical calculation of time dependent viscous incommpressible flow with free surface*, Physics and Fluids **8** (1965), 2182–2189.
29. A. Henderson, *ParaView guide, a parallel visualization application.*, Kitware Inc., 2007.

30. J. O. Hirschfelder, C. F. Curtiss, and R. B. Bird, *Molecular theory of gases and liquids*, John Wiley and Sons,, New York, 1954.
31. R. Holtzman, D. B. Silin, and T. W. Patzek, *Mechanical properties of granular materials: A variational approach to grain-scale simulations*, International Journal for Numerical and Analytical Methods in Geomechanics **33** (2009), no. 3, 391–404.
32. Pavel Iassonov, Thomas Gebrenegus, and Markus Tuller, *Segmentation of X-ray computed tomography images of porous materials: A crucial step for characterization and quantitative analysis of pore structures*, Water Resour. Res. **45** (2009), no. 9, W09415–.
33. F. Javadpour, *Nanopores and apparent permeability of gas flow in mudrocks (shales and siltstone)*, Journal of Canadian Petroleum Technology **48** (2009), no. 8, 16–21.
34. E. Jettestuen, J. O. Helland, and M. Prodanović, *A variational level set method for simulation of capillary-controlled displacements*, XIX International Conference on Water Resources CMWR June 17-22, 2012, University of Illinois at Urbana-Champaign, 2012.
35. G. Jin, T.W. Patzek, and D. B. Silin, *Physics-based reconstruction of sedimentary rocks. SPE 83587*, SPE Western Regional / AAPG Pacific Section Joint Meeting (Long Beach, California, U.S.A.), SPE, 2003.
36. ———, *Direct prediction of the absolute permeability of unconsolidated and consolidated reservoir rock. SPE 90084*, 2003 SPE Annual Technical Conference and Exhibition (Houston, Texas, U.S.A.), SPE, 2004.
37. L. J. Klinkenberg, *The permeability of porous media to liquids and gases*, Drilling and Production Practice, American Petroleum Institute, 1941.
38. M. N. Kogan, *Rarefied gas dynamics*, Plenum Press, New York, 1969.
39. L. D. Landau and E. M. Lifschitz, *Fluid mechanics*, Series in advanced physics, vol. 6, Addison-Wesley, Reading, MA, 1959.
40. M. C. Leverett, *Flow of oil-water mixtures through unconsolidated sands*, Trans. AIME **132** (1939), 381–401.
41. ———, *Capillary behavior in porous solids*, Trans. AIME **142** (1941), 152–169.
42. C. Manwart, U. Aaltosalmi, A. Koponen, R. Hilfer, and J. Timonen, *Lattice-Boltzmann and finite-difference simulations for the three-dimensional porous media*, Physical Review E **66** (2002), 016702 1–11.
43. N. S. Martys and H. Chen, *Simulation of multicomponent fluids in complex three-dimensional geometries by the lattice Boltzmann method*, Physical Review E **53** (1996), 743.
44. J. C. Maxwell, *On stresses in rarefied gases arising from inequalities of temperature*, Philos. Trans. Royal Soc. London **170** (1879), 231–256.
45. M. Muskat and M. W. Meres, *The flow of hetereogeneous fluids through porous media*, Physics **7** (1936), 346–363.
46. P. E. Øren and S. Bakke, *Process based reconstruction of sandstones and prediction of transport properties*, Transport in Porous Media **46** (2002), no. 2-3, 311–343.
47. P. E. Øren, S. Bakke, and H. G. Rueslåtten, *Digital core laboratory: Rock and flow properties derived from computer generated rocks*, International Symposium of the Society of Core Analysts (Trondheim, Norway), Society of Core Analysits, 12-16 September 2006.
48. T. W. Patzek, *Verification of a complete pore network simulator of drainage and imbibition*, SPE Journal **6** (2001), no. 2, 144–156.
49. Maša Prodanović and Steven L. Bryant, *A level set method for determining critical curvatures for drainage and imbibition*, Journal of Colloid and Interface Science **304** (2006), no. 2, 442 – 458.
50. S. Rassenfoss, *Digital rocks out to become a core technology*, Journal of Petroleum Technology (2011), 36–41.

51. Franoise Rouquerol, Jean Rouquerol, and Kenneth Sing, *Adsorption by powders and porous solids. Principles, methodology and applications*, Elsevier, 1999.
52. Subrata Roy, Reni Raju, Helen F. Chuang, Brett A. Cruden, and M. Meyyappan, *Modeling gas flow through microchannels and nanopores*, Journal of Applied Physics **93** (2003), no. 8, 4870–4879.
53. A. A. Samarskii, *Theory of difference schemes*, Marcel Dekker Inc, N.Y., 2001.
54. J. Schembre-McCabe, R. Salazar-Tio, G. Ball, and J. Kamath, *A framework to validate digital rock technology. SCA2011-28*, International Symposium of the Society of Core Analysts held in Austin, Texas, USA 18-21 September, 2011 , 2011.
55. Will Schroeder, Ken Martin, and Bill Lorensen, *The Visualization Toolkit, Third Edition*, Kitware Inc.
56. Mehmet Sezgin and Bülent Sankur, *Survey over image thresholding techniques and quantitative performance evaluation*, J. Electron. Imaging **13** (2004), 146–165.
57. Keith W. Shanley, Robert M. Cluff, and John W. Robinson, *Factors controlling prolific gas production from low-permeability sandstone reservoirs: Implications for resource assessment, prospect development, and risk analysis*, AAPG Bulletin **88** (2004), no. 8, 1083–1121.
58. M. Shashkov, *Conservative finite-difference methods on general grids*, CRC Press, Roca Baton, FL, 1996.
59. D. Silin and T. Patzek, *Pore space morphology analysis using maximal inscribed spheres*, Physica A. Statistical Mechanics and its Applications **371** (2006), 336–360.
60. D. B. Silin and T. W. Patzek, *Support-operators method in the identification of permeability tensor orientation*, SPE Journal **6** (2001), no. 4, 385–398.
61. D. B. Silin and T. W. Patzek, *An object-oriented cluster search algorithm*, Tech. Report LBNL-51599, Lawrence Berkeley National Laboratory, 2003.
62. ———, *Predicting relative-permeability curves directly from rock images. SPE 124974*, 2009 SPE Annual Technical Conference and Exhibition (New Orleans, Louisiana, U.S.A.), SPE, 2009.
63. Dmitriy Silin, Timothy J. Kneafsey, Jonathan B. Ajo-Franklin, and Peter Nico, *Pore-scale mechanisms of gas flow in tight sand reservoirs*, Tech. Report LBNL-4103E, Lawrence Berkeley National Laboratory, November 2010.
64. ———, *A multimodal 3D imaging study of natural gas flow in tight sands. SPE paper 146611*, SPE Annual Technical Conference and Exhibition, 30 October-2 November 2011, Denver, Colorado, USA, 2011.
65. Dmitriy Silin, Liviu Tomutsa, Sally Benson, and Tad Patzek, *Microtomography and pore-scale modeling of two-phase fluid distribution*, Transport in Porous Media (2010), 1–21, 10.1007/s11242-010-9636-2.
66. Cecilia Solar, Andrés García Blanco, Andrea Vallone, and Karim Sapag, *Adsorption of methane in porous materials as the basis for the storage of natural gas*, Natural Gas (Primoz Potocnik, ed.), Sciyo, August 2010, pp. 205–244.
67. P. Spanne, J. F. Thovert, C. J. Jacquin, W. B. Lindquist, K. W. Jones, and P. M. Adler, *Synchrotron Computed Microtomography of Porous Media: Topology and Transports*, Phys. Rev. Lett. **73** (1994), no. 14, 2001–2004.
68. A. N. Tikhonov and A. A. Samarskii, *Equations of mathematical physics*, International series of monographs in pure and applied mathematics; v. 39, Macmillan, New York, 1963.
69. Liviu Tomutsa and Velimir Radmilovic, *Focused ion beam assisted three-dimensional rock imaging at submicron scale, SCA2003-47*, International Symposium of the Society of Core Analysts (Pau, France), September 2003.
70. Liviu Tomutsa, Dmitriy Silin, and Velimir Radmilovic, *Analysis of chalk petrophysical properties by means of submicron-scale pore imaging and modeling*, SPE Reservoir Evaluation and

Engineering **10** (2007), no. 3, 285–293.

71. Olga I. Vinogradova, *Drainage of a thin liquid film confined between hydrophobic surfaces*, Langmuir, 1995, 11 (6), pp 22132220 **11** (1995), no. 6, 2213–2220.
72. Olga I. Vinogradova and G. E. Yakubov, *Surface roughness and hydrodynamic boundary conditions*, Physical Review E **73** (2006), no. 4, 045302.
73. I. V. Volkov and O. G. Fridlender, *Boundary conditions of gas dynamic slip on a rough surface*, Fluid dynamics **22** (1987), no. 1, 156–159.
74. G. Voronoi, *Nouvelles applications des paramètres continus à la théorie des formes quadratiques*, Journal für die reine und angewandte Mathematik **133** (1907), 97–178.